FABRICATION OF POLARIZATION-MAINTAINING OPTICAL FIBER WITH ULTRA-LOW BENDING-DEPENDENT POLARIZATION EXTINCTION RATIO DETERIORATION

A THESIS SUBMITTED TO

THE GRADUATE SCHOOL OF ENGINEERING AND SCIENCE

OF BILKENT UNIVERSITY

IN PARTIAL FULFILLMENT OF THE REQUIREMENTS FOR

THE DEGREE OF

MASTER OF SCIENCE

IN

MATERIALS SCIENCE AND NANOTECHNOLOGY

By

Samet Akçimen

February 2023

Fabrication of Polarization-Maintaning Optical Fiber with Ultra-Low Bending-Dependent Polarization Extinction Ratio Deterioration
By Samet Akçimen
February 2023

We certify that we have read this thesis and that in our opinion it is fully adequate, in scope and in quality, as a thesis for the degree of Master of Science.

Bülend Ortaç(Advisor)

Onur Tokel

Hakan Altan

Approved for the Graduate School of Engineering and Science:

Orhan Arıkan
Director of the Graduate School

ABSTRACT

FABRICATION OF POLARIZATION-MAINTAINING OPTICAL FIBER WITH ULTRA-LOW BENDING-DEPENDENT POLARIZATION EXTINCTION RATIO DETERIORATION

Samet Akçimen
M.S. in Materials Science and Nanotechnology
Advisor: Bülend Ortaç
February 2023

Polarization-Maintaining Optical Fiber (PM) is a unique-designed fiber that preserves and utilizes the polarization state of the light transmission that is launched into it. With this aspect, our biaxial PM fiber is adequate for different applications, including interferometers, fiber optic gyroscopes (FOGs), telecommunication, and all-PM fiber lasers by maintaining single polarized light transmission against the environmental perturbation. A biaxial PM fiber, which was found to possess high polarization extinction ratio (PER) values over 30 dB among two orthogonal axes, is composed of the unique geometry that is the combination of elliptical core and Panda-type PM fibers. Even under environmental temperature conditions, from -55 °C to +85 °C, the PER values were obtained to be maintained. During the bending dependent PER measurements, it was observed that the PER values at relatively small diameters from 12 mm to 5 mm were not altered compared to the biaxial PM fibers not bent. PER deterioration was determined as 0.5%. We measured the group beat lengths which were 1.40 mm for one axes and 1.45 mm for the other at 1550 nm to confirm the biaxial PM property. The optical loss of the biaxial PM fiber was measured with an optical time-domain reflectometer (OTDR) and the loss was found to be below 1.5 dB/km for over 3 km of fiber length. Along two polarized axes, the mode field diameter (MFD) and the numerical aperture (NA) values were also determined. This novel PM fiber addresses a need for the Panda and elliptical core type (PM) fibers which are essential for integrated fiber based sensors and instruments, such as fiber optic gyroscopes.

Keywords: Optical Fibers, Polarization Maintaining (PM), High-Birefringence, Beat Length, Elliptical Core, Panda-type, Fiber Optic Gyroscopes (FOGs).

ÖZET

ÇOK DÜŞÜK BÜKÜLMEYE BAĞLI POLARİZASYON SÖNÜMLENME ORANI KAYBIYLA ÇİFT EKSENLİ POLARİZASYON KORUMALI FİBER ÜRETİMİ

Samet Akçimen
Malzeme Bilimi ve Nanoteknoloji , Yüksek Lisans
Tez Danışmanı: Bülend Ortaç
February 2023

Polarizasyon-korumalı optik fiberler içine eşleştirilen ışığın polarizasyonunu fiber boyunca koruyan ve düşük kayıpla ileten özel tasarıma sahip fiberlerdir. PM fiberlerin bu tasarımsal özelliği ile elde edilen fiber boyunca tek bir polarize ışık iletimi interferometreler, fiber optik jiroskoplar, telekomünikasyon ve tüm PM fiber lazerler gibi PM fiber uygulamalarında ihtiyaç duyalan önemli bir gereksinimdir. İki ortogonal eksen arasında 30 dB'lik yüksek polarizasyon sönümlenme oranına (PSO) sahip yeni bir tür çift eksenli PM fiber üretildi. Tasarlanan bu fiber eliptik çekirdek ve Panda tipi fiberin kombinasyonuna sahiptir. PSO değerlerinin -55 °C ile +85 °C arasında çevresel sıcaklık koşullarında korunduğu gözlemlenmiştir. Bükülmeye bağlı kayıp ölçümleri, çift eksenli PM fiberin, 12 mm'den 5 mm'ye kadar çeşitli bükülme çaplarında çok düşük bükülmeye bağlı PSO bozulmasına (0.5%) sahip olduğunu göstermiştir. Çift eksenli PM özelliği, grup atım uzunluğu ölçümleriyle de desteklenmiş olup, 1550 nm'lik dalgaboyunda bir eksen için 1.40 mm ve diğer eksen için 1.45 mm olduğu elde edilmiştir. Optik zaman alanlı yansıtıcı (OTDR) ölçümleri, çift eksenli PM fiberin optiksel kaybının 3 km'lik uzunluk boyunca 1.5 dB/km'nin altında olduğunu göstermektedir. Mod alan çapı (MFD) ve sayısal açıklık (NA) değerleri de iki polarize eksen boyunca rapor edilmiştir. Bu yeni PM fiber, entegre fiber tabanlı sensörler ve ekipmanlar için kullanılan eliptik ve Panda tipi PM fiberler için bir çözüm sunmaktadır.

Anahtar sözcükler: Optik Fiberler, Polarizasyon-Koruma, Yüksek Çift Kırınım, Atım Uzaklığı, Eliptik Çekirdek, Panda-tipi, Fiber Optik Dönü Ölçer.

Acknowledgement

I would like to express my sincere gratitude to my supervisor, Assist. Prof. Dr. Bülend Ortaç who has been holding my hand, guiding and preparing me for the future from the last years of my undergraduate education till the end of graduate education. Therefore, I am conscious that I would be unable to succeed without his support, encouragement, and supervision. I would also like to thank my thesis committee members Assist. Prof. Dr. Onur Tokel and Prof. Dr. Hakan Altan for their contributions, advice, and guidance throughout this study.

I am deeply grateful for my dear Ortaç Group colleagues, first and foremost, Elif Yapar Yıldırım, Dr. Ali Karatutlu, and Dr. Esra Kendir. I am aware that this thesis could not have been completed without their generous support, graciousness, wholeheartedness, and dedicated involvement in all of the steps and moments in that I have encountered obstacles and difficulties.

I am appreciative to my soul mates, Anıl and Çağlar, whose presence I have always sensed for more than 10 years, even though we were unable to find the time or see each other frequently. I am also sincerely thankful for my great pals Doğukan Hazar Özbey, Mehmet Halit Öztürk, lab and flatmate Umut Taylan, office mates Mohammadali Razeghi, and Amir Parsi. They have been a source of joy, energy, and motivation for every single day during my master's degree.

I become speechless when it comes to her existence, Deniz Kanlı. I feel gratitude for her limitless love and patience. I would feel incomplete without her presence.

This thesis is dedicated to my dear mother Aysel, father Saadettin, and sister Gözde. I cannot thank them enough for providing me with a warm home environment and loving me unconditionally throughout my entire life.

The current study has been supported by the Scientific and Technological Research Council of Turkey (TUBITAK) under Project No. 20AG001.

Contents

List of Figures

List of Tables

Chapter 1

Introduction

Fibers are classified based on the types of refractive index profiles of the fiber core and the number of modes of propagation of light in the fiber. The improvement in propagation properties is considered another way to classify optical fibers [1]. Thus, polarization-maintaining (PM) fibers can be given as an example of a special type of single-mode fiber. Although polarization maintenance may be proven in any single-mode fiber under controlled circumstances as long as the fiber is preserved sufficiently short, straight, and protected from any form of environmental perturbation, problems are likely to occur when the fiber is employed in real-world applications [2]. At this point, PM fibers have attracted a great deal of interest and become critical optical fibers that transmit and deliver light along fiber by conserving the polarization state of light without being affected by environmental influence such as mechanical stress-related caused by micro-bending or macro-bending, temperature fluctuations, etc. [3, 4]. PM fibers become a greater concern when polarization maintenance is required for the applications of telecommunication, fiber optic gyroscopes (FOGs), biomedical field, and all-PM fiber lasers [3, 5–7], especially in harsh environmental conditions. Therefore, we provided high modal birefringence, which is considered the ability of preserving the polarization state and known as the effective index difference between the orthogonal polarization modes, based on both stress birefringence and geometrical birefringence. The stress birefringence is generated by the stress

rods while the geometrical birefringence is related to the asymmetry in the structural design of the core and the refractive index difference between the core and cladding [5].

Creating birefringence between the axes parallel and perpendicular to the direction of stress-applying parts (SAPs), where they generate a difference between the propagation constants of two orthogonally polarized eigenmodes ($\Delta\beta = \beta_x - \beta_y$), can be considered a method for overcoming probable perturbations that fiber may encounter. In this way, the polarization modes are forced to propagate at different velocities. In other words, as the applied stress increases, the difference in propagation constant between the two axes increases. This difference induces a permanent PM property on the fiber, resulting in significant birefringence without a significant deviation ($\pm$ 2 dB) so that optical energy cross-coupling becomes extremely difficult even under harsh environmental conditions [8, 9]. It is feasible to produce this difference in order to eliminate the degeneracy between the two polarization modes by modifying the azimuthal symmetry of PM fibers, such as by making the core highly elliptical shape to provide high-birefringent (Hi-Bi) property [2]. As the characteristic properties, such as mode field diameter (MFD), attenuation, and numerical aperture (NA), of the Panda-type PM fibers are taken into account, it is evident that the Panda-type PMFs match well with single-mode fibers (SMFs) used in telecommunications.

On the other hand, the symmetrical boron-doped stress-applying rods were placed independently within two drilled holes in the preform before the drawing process. A significant amount of B_2O_3 ($\geq$ 14 mol%) in the stress-applying rods (SARs) are used for the creation of stress difference between the SAPs and the fused silica cladding [10]. However, we used 5 mol% GeO_2-doped silica along the core and 20 mol% B_2O_3-doped silica along the SARs.

The fabrication of elliptical core fiber can be provided during the collapsing process of the preform fabrication in the MCVD process. The inner walls of the collapsing preform will have some degree of perturbation leading to ellipticity since the surface tension forces within the collapsing preform are not precisely balanced by applying pressure to the substrate. Therefore, the highly elliptical

core optical fiber preform can be obtained by removing the circularizing effect of the lathe's rotation and collapsing it under vacuum [11]. However, we formed the core of the fiber as a circular, elliptical, and highly elliptical core by adjusting the temperature as $T_1 = 1950$ °C, $T_2 = 1970$ °C, and $T_3 = 1990$ °C respectively in the initial part of the fiber drawing process. This indicates that the shape of the PM fiber core can be changed and controlled by applying different temperatures while all other drawing parameters (drawing speed of 15 m/min, etc.) are maintained constant. In this way, we could obtain the combination of conventional Panda-type PM fiber and elliptical core, including the SAPs with a diameter of $\varnothing_{SAP} \approx 25$ μm. Thus, it can be concluded that not only the maximum lateral stress level established in this study is greater compared to that represented in the preceding article [10] but also the biaxial birefringence values around two orders of magnitude are higher than the birefringence calculated [12].

Consequently, in this thesis, a Hi-Bi biaxial PM fiber possessing the properties of both Panda-type and elliptical-core PM fiber was proposed to preserve the polarization state of transmitted light against external perturbations along the so-called slow axis and prevent cross-coupling between this axis and the fast axis. This thesis also analyzes the development of a biaxial PM fiber with SAPs and an elliptical core by cautiously controlling the fabrication parameters. This caution enabled the PERs along two-orthogonal axes to be maintained over 30 dB over a fiber length of 110 m at harsh temperature conditions from -55 °C to +85 °C with ultra-low PER deterioration.

Chapter 2

Theoretical Background

In this chapter, I will describe the general principles of optical fibers and waveguides, as well as the working principle of the process of total internal reflection (TIR), the most prevalent fiber types, the effect of polarization and interference in optical fibers, and the application field of PMF.

2.1 Basic principles of optical fibers

An optical fiber consists of a unique-designed geometry. The layered structure contains a core, cladding, and plastic protective coatings [13] which all have different refractive indices. The inner portion of the fiber called the core is surrounded by a transparent material called the cladding, as illustrated respectively in **Fig. 2.1a** and **2.1b** as a schematic illustration of the side view and cross-sectional area of optical fiber. The core region has a higher refractive index than the cladding region, as the **Fig. 2.1c** points out. To preserve the waveguide property, the glass rod structure (rode and cladding) is coated with low-index acrylic polymer. Therewith, as a final step, the mechanical property is provided by re-coating the entire structure with high-index polymer in order to maximize fiber strength and micro-bending resistance [2].

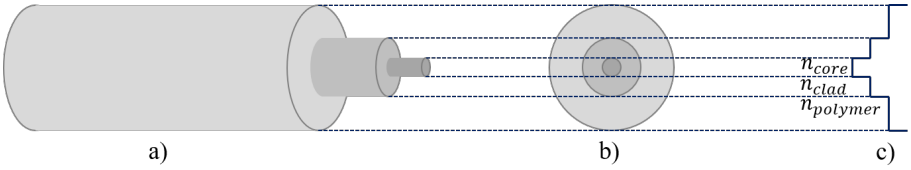

Figure 2.1: (a) The schematic representation of side view of optical fiber (b) cross-sectional area of the fiber core, clad, and coating from the inside out respectively (c) the refractive index profile of the fiber.

2.1.1 Optical fibers as a waveguide

2.1.1.1 Transmission

In fiber optics, light is transmitted in the form of rays [14]. The refractive index difference between the core and cladding serves the ray of launched light not to escape from the core to the cladding region [15]. When a ray of light propagates in an optical fiber, it follows Snell-Descartes' law which states that the ratio of the sines of the angles of incidence and refraction is a constant as given in **Eqn. 2.1** [16–19].

$$n_1 sin\theta_1 = n_2 sin\theta_2 \tag{2.1}$$

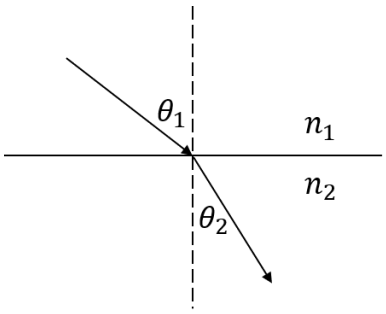

Figure 2.2: A light ray moving from a medium with an index of refraction n_1 into another with an index of refraction n_2.

The light in an optical fiber hits the interface from the region with the higher refractive index and is completely reflected inside the optical fiber by the phenomenon of total internal reflection (TIR). It occurs when the incidence angle θ_1 is more the critical angle θ_c which is the case of corresponding to 90° angle of refraction (θ_2=90°), as shown in **Eqn. 2.2** and **2.3**. A ray of light, therefore, is preserved in the core, captured, and transmitted all along the fiber. Besides, at the critical angle, the light only propagates through the interface of the two mediums, as in **Fig. 2.3a**.

$$n_1 sin\theta_c = n_2 sin90° \tag{2.2}$$

$$\theta_c = arcsin\left(\frac{n_2}{n_1}\right) \tag{2.3}$$

When the critical angle θ_c is exceeded, the entire light energy remains propagating in the medium with the higher optical density, and none of it is refracted in the other medium [20] as in **Fig. 2.3b**.

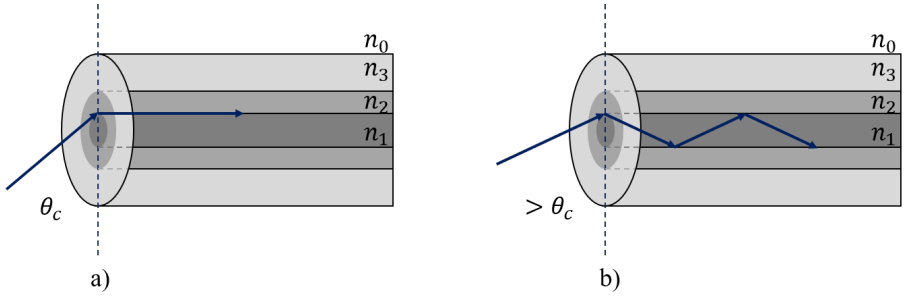

Figure 2.3: The schematic design of the light propagation inside the optical fiber (a) at the interface between the two media (b) when total internally reflected.

2.1.1.2 Numerical aperture

Each fiber is capable of gathering light through its core. The maximum acceptance value of the entrance angle of fiber θ_{max}, however, is restricted by the limit between reflection and refraction. As stated in the previous chapter, this limit is determined by the critical angle, which is related to a parameter known as the numerical aperture (NA), as given in **Eqn. 2.4**. and **2.5**.

$$NA = \sqrt{n_{core}^2 - n_{clad}^2} = sin\theta \tag{2.4}$$

$$\theta = arcsin\left(\frac{1}{n_0}\right)\sqrt{n_{core}^2 - n_{clad}^2} \tag{2.5}$$

where θ represents the angle of an imaginary acceptance cone. It defines the maximum angle of incidence and how much light will be gathered by the fiber [21,22]. The full acceptance cone is defined as 2θ as it is shown in **Fig. 2.4**.

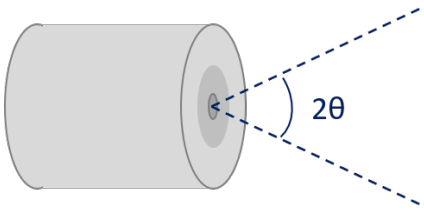

Figure 2.4: The corresponding drawing of the fiber's acceptance angle.

2.2 Types of optical fiber

Optical fibers vary in their modes of propagation of light, refractive index, and materials used.

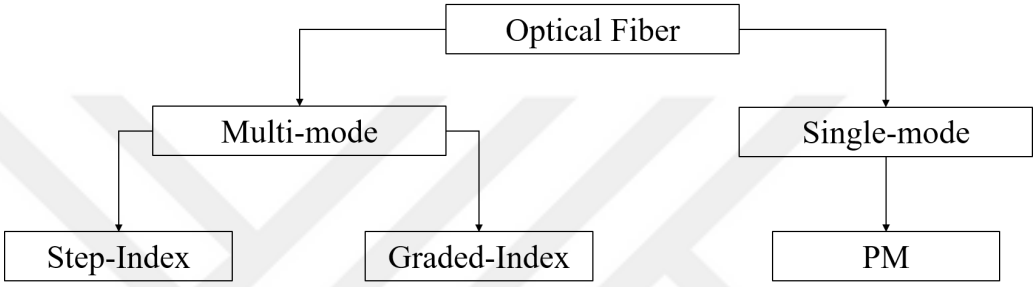

Figure 2.5: Types of optical fiber

2.2.1 Multi-mode fiber

Multi-mode fibers have a larger core diameter compared to single-mode fibers. Thus, the higher-order modes can propagate through the waveguide. The index of refraction of the core is higher than that of the cladding. Multi-mode fibers, also, provide an easier way of coupling the light into the fiber core [1].

2.2.1.1 Step-index Multi-mode fiber

The refractive index of Step-index Multi-mode fibers is uniformly distributed along the core of the fiber, as indicated by its name. The light guided along the optical fiber follows the phenomenon of total internal reflection (TIR). As long as the incidence angle of light (θ_1) is more than the critical angle (θ_c), the entire light energy remains propagating in the medium with higher optical density i.e., the core of the fiber.

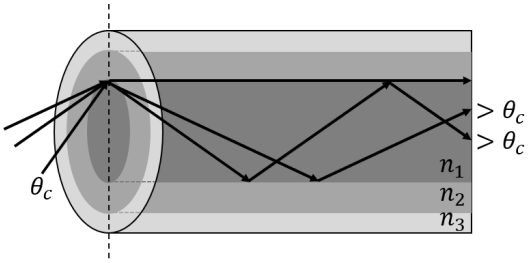

Figure 2.6: The representation of Step-index Multi-mode Fiber

2.2.1.2 Graded-index Multi-mode fiber

Graded-index multi-mode fibers have a special fiber design where the refractive index is highest in the fiber core. As it refers to the fact that the refractive index gradually decreases from the center of the core to the outer of the core and reaches its lowest value at the interface between the cladding and the core. As a result, the light rays near to interface travel faster. However, the radial reduction of refractive index causes light rays that propagate through the relatively less refractive index of medium to bend back towards to center of the core [23]. Unlike the step-index multi-mode fiber, the graded-index multi-mode fiber follows a serpentine path rather than the phenomenon of total internal reflection (TIR). Therefore, it is concluded that all modes reach the end of the fiber at about the same time by reducing modal dispersion considerably compared to step-index multi-mode fibers [4].

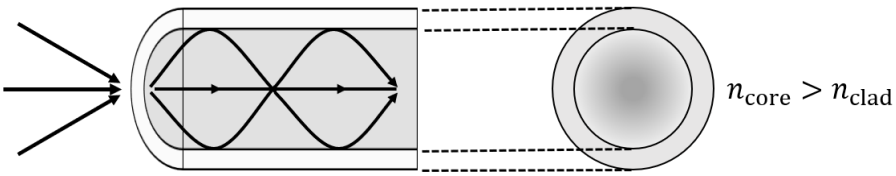

Figure 2.7: The representation of Multi-mode Graded-index Fiber

2.2.2 Single-mode fiber

The term single-mode refers to the fact that a single-mode fiber transmits only the fundamental zero-order mode of propagation, LP_{01}. It is maintained in the V number (the normalized spatial frequency) of the waveguide is less than 2.405 which is the single-mode operation threshold value for an optical fiber [2, 24].

Figure 2.8: The representation of Single-mode Step-index Fiber

The V number is related to the acceptance angle and numerical aperture of the fiber expressed by,

$$V = \frac{2\pi a}{\lambda} sin\theta = \frac{2\pi a}{\lambda} NA \tag{2.6}$$

where a is the core radius of the fiber. Step-index single-mode fiber is also characterized by the cutoff wavelength, as defined in **Eqn. 2.7**.

$$\lambda_c^{th} = \frac{2\pi n_1 a\sqrt{2\Delta}}{2.405} \tag{2.7}$$

where n_1 is the refractive index of the core and Δ is the relative index difference between the core and cladding. The theoretical cutoff wavelength, ${\lambda_c}^{th}$, of a single mode fiber is the wavelength above which only the fundamental LP_{01} mode propagates [25]. In other words, it is the wavelength above in which a fiber acts as a single-mode fiber [26, 27]. Below the cutoff wavelength, LP_{11} and other higher-order modes propagate, and fiber becomes a multi-mode fiber.

The single-mode fibers have a significantly smaller core size and are utilized for long-range signal transmission. Unlike in the multi-mode fibers, the dispersion caused by multiple modes are not occurred in the single-mode fibers [4]. Thus, they are capable of carrying higher bandwidths.

2.2.2.1 Polarization Maintaining Fiber

Polarization-maintaining fibers are mostly considered a special type of single-mode fibers (only in rare cases few-mode fibers [28]), where the linear polarization of the linearly polarized light is preserved during propagation. Most commercially available PM fibers consist of three different stress-birefringent geometry categories: bow-tie, PANDA, or elliptical core fiber. The three versions, as presented in **Fig. 2.9**, all serve the same primary function of preserving the polarization by generating sufficient birefringence so as to reduce the optical power interchange between polarization modes [29].

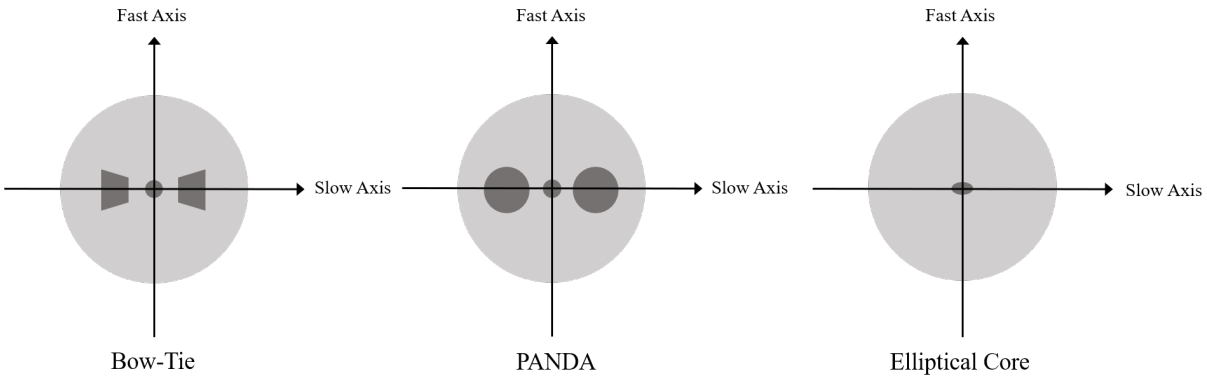

Figure 2.9: Cross-section of Bow-Tie, PANDA, and Elliptical Core PM fiber geometries respectively

The fiber core maintains birefringence induced by tension while the fiber preform is drawn. The direction of the applied stress results in the formation of two distinct refraction indices. A higher index is parallel to the direction of the stress, and a lower index is perpendicular to it [2].

2.3 Polarization and Interference Effect in Optical Fiber

Light is a special kind of electromagnetic energy whose propagation through space can be described by wave motion [30]. As light waves are electromagnetic waves, they are comprised of two components: electric fields and magnetic fields whose components of amplitudes oscillate periodically through time and space, as presented in **Fig. 2.10**. The direction the wave propagates is at a right angle to the direction of the electric and magnetic fields [4].

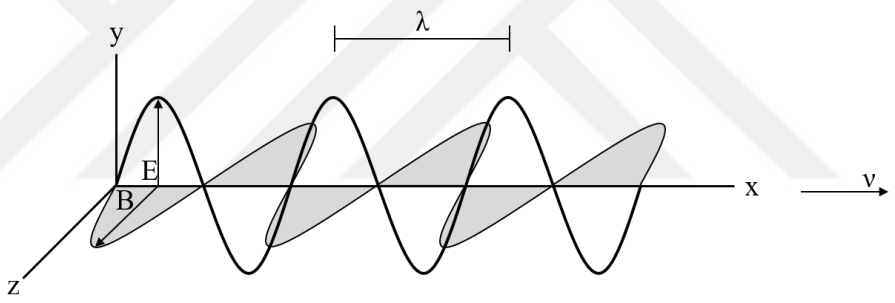

Figure 2.10: Electric and magnetic field vectors of the polarized light wave traveling along the x axis.

The solutions of the wave equation of a plane wave, propagating in the direction of the vector $\vec{k}$, can be described as;

$$\vec{E} = \vec{E_0}\cos(\vec{k}.\vec{x} - \omega t + \phi_0) \tag{2.8}$$

$$\vec{B} = \vec{B_0}\cos(\vec{k}.\vec{x} - \omega t + \phi_0) \tag{2.9}$$

where $\vec{E_0}$ and $\vec{B_0}$ are constant vectors, ϕ_0 is a constant phase, ω is the angular frequency, and $\vec{k}$ is the wave vector.

Polarization is an important phenomenon induced by the wave nature of electromagnetic radiation, and it defines the geometrical orientation of the oscillations [31]. Polarization is the phenomenon in which the vector vibrations of light are confined to a particular direction in a plane. The direction of the electric field (and magnetic field) vector that oscillates perpendicularly to the direction of propagation is defined as the polarization direction. The polarization of the light waves, therefore, is referred to as transverse waves. In contrast to the non-transverse waves, they are limited to wave propagation [32–34].

Polarized and unpolarized light are two significant forms of light. If light consists of electromagnetic waves all aligned in one direction compared to the propagation of light, such light is called as linearly polarized light as shown in **Fig. 2.11a**. In addition to linear polarization, if light consists of waves that are all continuously rotating in the same direction with an exact $\pi/2$ phase difference between the oscillation of the two orthogonal field components, it is referred to as circularly polarized light, as presented in **Fig. 2.11b**. Besides, circularly polarized waves can be considered to be composed of two linearly polarized waves oscillating perpendicularly [35]. If the phase difference between two plane waves differs from $\pi/2$, then the light is referred to as elliptically polarized light as the **Fig. 2.11c** points out. The elliptical light can alternatively be conceived as the sum of linearly and circularly polarized waves [35]. On the other hand, if a light is formed of electromagnetic waves that are oriented in all different directions, it is referred to as unpolarized light and is presented in **Fig. 2.11d**.

As the light propagates through the fiber, the polarization state of the light is not normally maintained by a single-mode optical fiber, resulting in the fiber being extremely sensitive to any perturbation that the fiber encounters. Therefore, due to the lack of single-polarization fibers, research has focused on identifying the various birefringence mechanisms that can exist or be induced in a fiber [36]. Single-mode fibers allow two orthogonally polarized modes that have nearly identical propagation constants, meaning they propagate at the same velocity [37,38]. Therefore, the optical energy transition from one mode to the other would be easy if the light faced any form of perturbation or asymmetry within the fiber. At this point, the importance of polarization-maintaining fibers emerges since

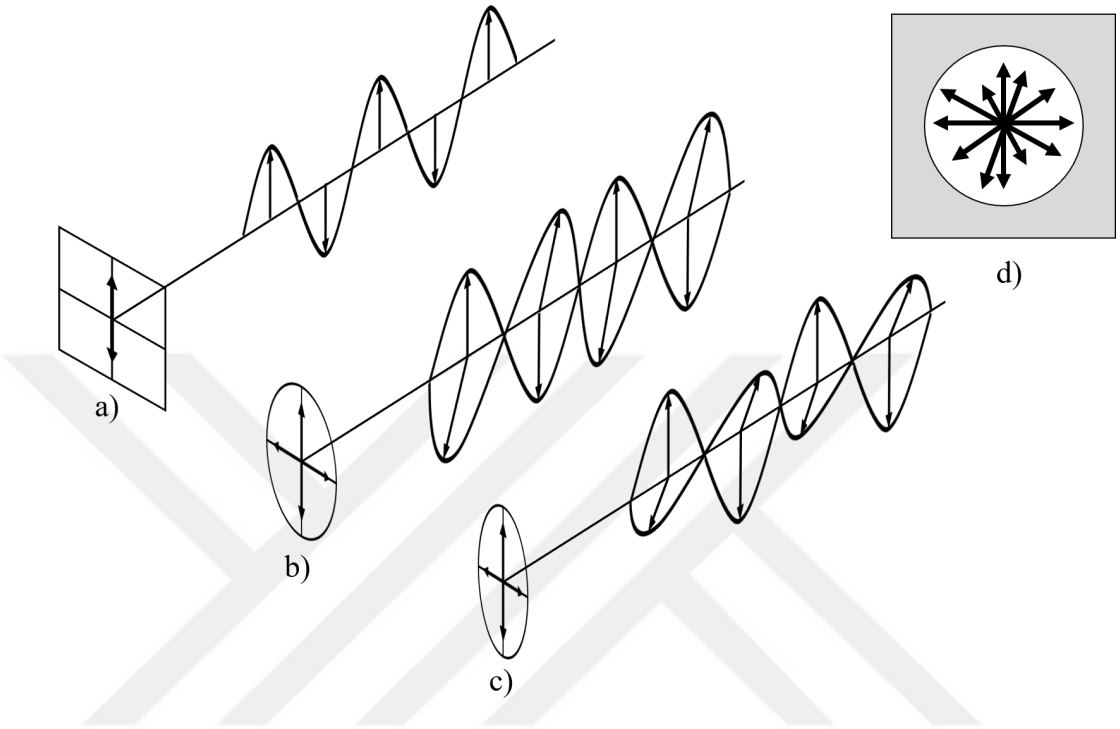

Figure 2.11: The representation of types of light polarization (a) linearly polarized light (b) circularly polarized light (c) elliptically polarized light (d) unpolarized light

the two orthogonally polarized modes are forced to possess different propagation constants [12]. The cross-coupling of optical energy becomes very difficult due to the mismatch in velocities; therefore, the state of polarization (SOP) of the transmitted light is maintained as the light was initially coupled to one of the principal axes of the fiber.

On the other hand, interference of light can be described as the variation of the intensity where multiple light waves superpose to form the resultant wave at a given position and time [39]. Numerous contemporary fiber optic components, such as Bragg gratings, wavelength-division multiplexing (WDM), optical filters, and so forth, exploit the phenomenon of interference.

If two light waves combine perfectly, i.e., they have the same wavelength and are in phase, they construct a wave that is the sum of the amplitudes of the incident waves. This phenomenon is known as constructive interference as shown in **Fig. 2.12**.

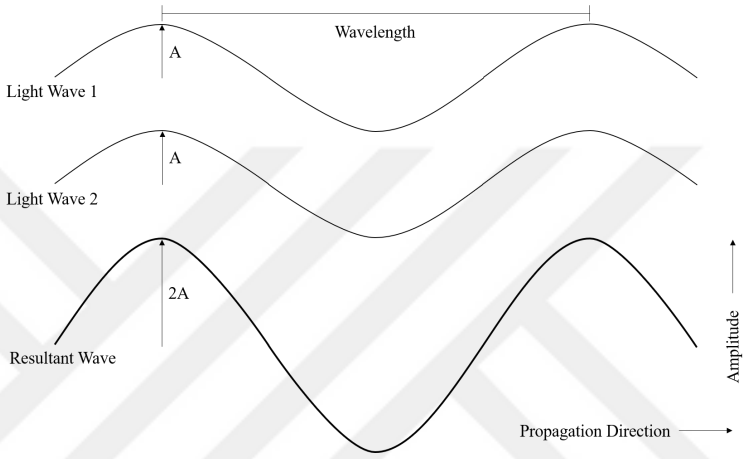

Figure 2.12: The schematic representation of constructive interference of two waves

If two waves are out of phase, let's say one is π-shifted, they cancel each other out. This is referred to destructive interference, as illustrated in **Fig. 2.13**.

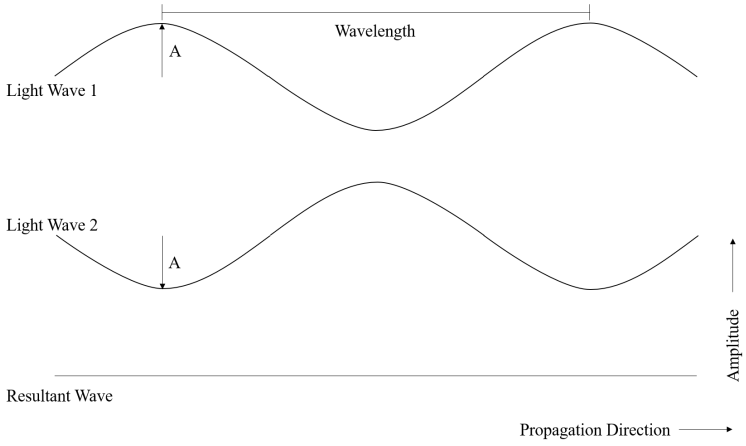

Figure 2.13: The schematic representation of destructive interference of two waves

So herewith, the polarization and interference phenomena, which affect the behavior of light, have the importance of taking up modern fiber optic components comprehensively.

2.4 Applications of PMF

PM fibers have a wide range of industrial uses that include telecommunications, medicine, and sensors. These applications are often interferometric and utilize the ability of the fiber to prevent signal loss in a way of sustaining that light traveling in the interferometer's signal and reference arms always are recombined with the same polarization state, resulting in optical constructive. However, the situation would be different, if the standard single-mode fiber (SMF) was utilized since the polarization state of the light propagating through each arm of the interferometer would range independently with respect to time and it would result in the recombination of the signal being faded [11]. For instance, a liquid level sensor based on PM fiber modal interferometer with waist-enlarge-splicing has been fabricated and showed the relations between wavelength shift and liquid level for three different refractive indices of liquids, as proposed in [40]. Also, D-shaped PM fiber can be used as a fiber optic sensor for the simultaneous monitoring of strain and the surrounding temperature, as presented in [41]. Furthermore, the tapered PMFs can be utilized as a high-sensitive acoustic sensor based on a microfiber Mach-Zehnder interferometer (MMZI), as stated in [42].

2.4.1 Interferometric Fiber Optic Gyroscope (IFOG)

One of the most commercial successes and extensive usage areas of PM fibers is the fiber optic gyroscope [43]. Interferometric Fiber Optic Gyroscope (IFOG) has been under development for several decades. They are utilized as rotation and rotation-rate sensors [2, 44, 45]. Three coils of PM fiber and three accelerometers constitute the inertial measurement unit (IMU) which is the system that estimates position, angular velocity, and linear acceleration [46].

2.4.1.1 Principle of the Fiber-Optic Gyroscope

The working principle of FOG is based on the Sagnac effect as presented in **Fig. 2.14a**. The Sagnac effect states that if there are two light waves counter-propagating through the closed loop, a phase difference is produced by rotation [47]. If there is no rotation applied to the system, two light waves propagating through the fiber coil in opposite directions will appear simultaneously at the end. Their paths taken are also equal in length. However, the light waves experience different fiber path lengths and different propagation times relatively as the fiber coil rotates about its symmetry axis as presented in **Fig. 2.14b**.

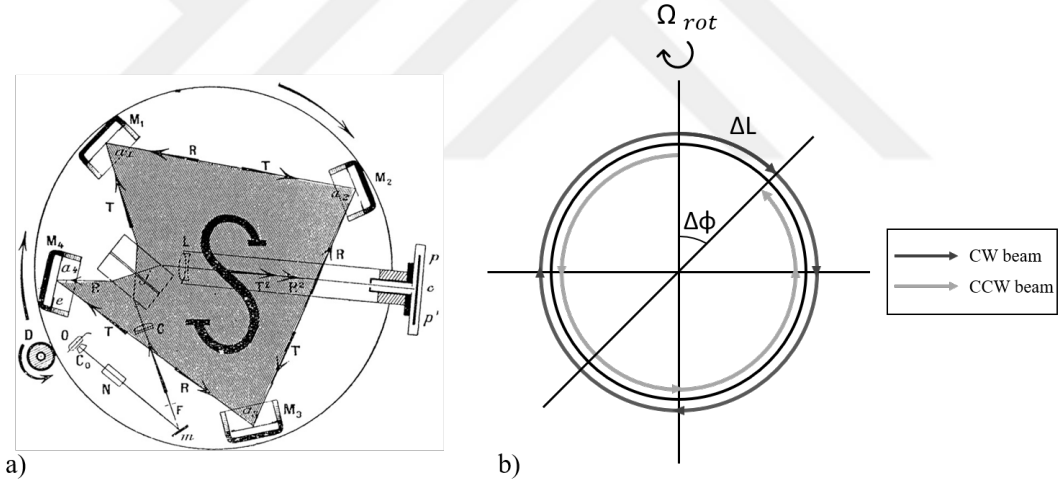

Figure 2.14: (a) Sagnac's original setup of a ring interferometer (b) Schematic diagram of Sagnac Effect under rotation Ω

The relative phase difference $\Delta\phi$ is proportional to the rotation rate Ω which is externally applied to the system. This phase difference creates a shift in the pattern of fringes detected by photo-detector [48]. One can define the path lengths taken by clockwise and counter-clockwise beams due to rotation as $L_{cw} = 2\pi R + R\Omega t_{cw}$ and $L_{ccw} = 2\pi R - R\Omega t_{ccw}$ respectively. Therefore, the difference in time required for each wave to complete one turn will be,

$$t_{cw} = \frac{R(2\pi + \Omega t_{cw})}{c} \tag{2.10}$$

$$t_{ccw} = \frac{R(2\pi - \Omega t_{ccw})}{c} \tag{2.11}$$

where R is the radius of the fiber coil, c is the velocity of light in vacuum, Ω is the rotation rate, and t_{cw} and t_{ccw} are travel times of clockwise (CW) and counter-clockwise (CCW) waves respectively.

One can solve t_{cw} and t_{ccw} separately and infer that the transit times differ by,

$$\Delta t = t_{cw} - t_{ccw} \tag{2.12}$$

$$\Delta t = 4\pi \frac{R}{c} \left(\frac{R\Omega}{c} \right) \tag{2.13}$$

Taking the wave transmission times with a coil of N turns into consideration,

$$\Delta t = 4\pi \frac{RN}{c} \left(\frac{R\Omega}{c} \right) \tag{2.14}$$

By substituting coil length L = 2πRN, coil diameter D = 2R, and $\Delta\phi = w\Delta t$ where w is the angular frequency of a light wave as denoted w = $2\pi c/\lambda$, the phase difference between the waves owing to the Sagnac effect is derived in **Eqn. 6.6**.

$$\Delta\phi_{Sagnac} = \frac{2\pi LD}{\lambda c}\Omega \tag{2.15}$$

As it is seen in the above-stated equation, the relative phase difference $\Delta\phi$ is proportional to the rotation rate Ω with a constant. The ratio between the change in sensor output and the relevant angular velocity variation is named as Sagnac Scale Factor (SF) [49]. This linear coefficient is denoted by,

$$SF = \frac{\Delta\phi_{Sagnac}}{\Omega} = \frac{2\pi LD}{\lambda c} \tag{2.16}$$

2.4.1.2 IFOG construction and components

A rotation rate sensing setup consists of a light source to create light waves, a coupler to direct and split the light waves, a fiber coil to observe the Sagnac effect, a multifunctional integrated optical chip (MIOC) to enable phase modulation, and a photodetector to sense the optical power.

In the fundamental IFOG architecture, it is essential to ensure the reciprocal configuration between CW and CCW waves. In contrast, two light waves at the photo-detector exhibit a phase shift of π when the system is at rest since the beam splitter induces a phase shift of $\pi/2$ between transmitted and reflected beams. This criterion can be achieved by adopting the so-called reciprocal configuration to the optical system, as presented in **Fig. 2.15**. Two optical signals, therefore, have the same amount of reflections and transmissions. Consequently, they end up arriving at the photodetector in phase [50].

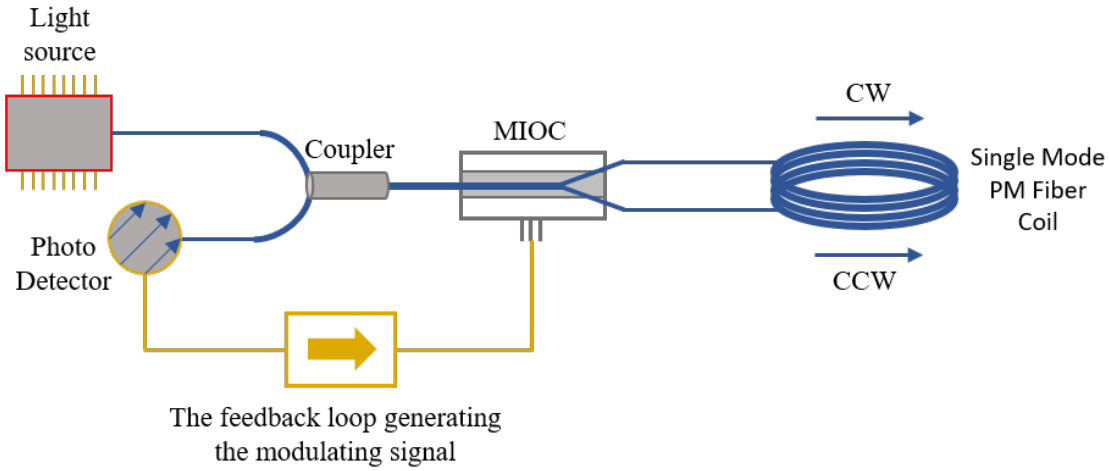

Figure 2.15: The most basic reciprocal configuration of IFOG

The use of a broadband light source with a short coherence length, such as superluminescence diode (SLD) [51] or a back-scattered amplified spontaneous emission (ASE) source with Er^{+3} doped fiber with an emission around 1550 nm and a pump of 980 nm [9], is the key important occurrence for IFOG to reduce errors caused by optical non-linearities [52]. Especially rare-earth doped fiber ASE sources provide a very high amplification gain, a high scale factor accuracy with wavelength stability, and high-power broadband emission since rare-earth energy levels are much more stable than those of semiconductors [43, 53, 54]. Hereby, Rayleigh-back-scattering noise can be considerably minimized.

It is noticeable that conserving a linear state of polarization against external perturbations and preventing cross-coupling from the slow axis to the fast axis are the essential steps toward a compact and practical IFOG device [43]. This functionality can be provided in IFOGs by employing PM fibers with stress-induced birefringence [9]. With the use of a broadband light source, as already stated and polarization-maintaining fiber, the residual birefringence-induced bias errors are reduced by careful gyroscope design that is crucial for good performance [55].

One of the essential components of IFOG is the couplers used for directing, splitting, and recombining the waves propagating in the IFOG system. The purpose of the first coupler in **Fig. 2.15** is to direct optical power generated by the light source toward to integrated optical circuit which separates light into CW and CCW waves to the traverse loop and recombines the returning waves in backward paths. Multi-functional integrated optic chip (MIOC) performs as a second Y-coupler (Lithium niobate, $LiNbO_3$-based Y junction waveguide structure) to ensure the reciprocal configuration. Besides, MIOC serves as a phase modulator, and a polarizing waveguide to eliminate the polarization non-reciprocity error. The working principle of MIOC is based on the electrical-optic effect of the crystal. For the modulation process, the electric field is applied to the substrate and withdrawn again which results in changing the refractive index of the crystal. The transmission characteristics of the substrate, therefore, are influenced. This modulation is regarded as the response to the closed loop feedback signal of the system [49, 56].

The result of the interference between two counter-propagating waves is processed as an optical signal at the photodetector to detect the Sagnac phase shift. The optical power is converted by the detector into electrical power. When considered from this point of view, the detector quantum efficiency, $\eta = \dot{N}_e/\dot{N}_p$ (where $\dot{N} = dN/dt$ is any flow yielding a random counting, $\dot{N}_p$ is the flow of photons per second, and $\dot{N}_e$ is the number of primary current of electrons per second), must be as close as possible to 1 in order have high quantum efficiency [43].

2.4.1.3 Optical Difficulties of IFOG and Solution Techniques

It is stated that encountering crucial optical problems in the operation of IFOG systems is inevitable, even in a perfectly reciprocal system [43]. These optical difficulties can be caused by other nonreciprocal effects, such as the Shupe effect, the nonlinear Kerr effect, or the magneto-optic Faraday effect. As it is required to have higher gyroscope performance grades, error sources and limitations should be explored conscientiously.

The Shupe effect is considered one of the main performance limitations affecting the accuracy of the fiber-optic gyroscopes. It is occurred by a thermally induced nonreciprocity in the fiber coil when there is a time-dependent temperature gradient along the fiber [57,58]. Since this effect results in the CW and CCW waves traversing a slightly different effective path and creating a thermal disturbance, a nonreciprocal phase shift is generated that becomes indistinguishable from the phase shift caused by rotation. However, the proper thermal modeling of the fiber coil by taking the efficient winding procedures (cylinder, symmetric, dipole, quadrupole, and octupole) into consideration provides to suppress the Shupe error as it enables to control the strain distribution through the fiber coil [59–61]. Selecting and controlling the coil geometrical factors, including the coil potted length, the adhesive layer thickness, the number of turns per layer, and the number of layers based on desired IFOG constraints elaborately serves to prevent any non-homogeneity created during the winding procedure [62, 63]. In addition to that, one can surround the fiber with insulating material to reduce thermal influences on the sensing fiber [64].

The Faraday effect is another major source of bias error in IFOGs, which causes the phase drift of the counter-propagating light waves passing through the fiber coil [43]. In an ideal optical fiber gyroscope positioned in a magnetic field that is perpendicular to the sensitive axis of the fiber coil, the fiber loop itself acts as a Faraday device [65]. Since the ideal circular single-mode fiber has uniformly rotated polarization along its entire length, the IFOG becomes completely insensitive to arbitrary magnetic fields. The phase difference between the CW and CCW light waves, therefore, is never generated [66]. In an actual IFOG with a single-mode fiber loop, however, the state of polarization changes unpredictably along the fiber. Thus, the phase difference appears due to polarization nonreciprocity (PNR) error induced by the Faraday effect in the fiber of coil [67]. The addition of polarization-maintaining fiber (PMF) and magnetic shield structure with a high shielding efficiency could be considered a reduction technique for the Faraday nonreciprocity [68,69]. In order to suppress the magnetic sensitivity, PM fibers can be utilized to provide the optical compensation in the dual-polarization IFOGs [70]. With the opposite polarities of the fluctuation between two orthogonal polarization states, which are mutually canceled by summing up their optical intensities, PNR errors are optically eliminated if the two polarizations have the same intensity and no coherence [71–75].

The Kerr effect is another important nonreciprocal effect that is originated by third-order electric polarization [76]. The intensity-dependent perturbations of the nonlinear index changes are defined as the optical Kerr effect. It is responsible for a significant rotation-rate error in the fiber-optic gyroscopes by causing an imbalance between the power levels of CW and CWW waves [77–79]. Due to the changes in propagation nonlinearity through the medium of the fiber core, CW and CWW waves may not have identical optical powers. Therefore, the unequal phase delay for counterpropagating waves appears as resulting from the different propagation constants that depend on the states of polarization of two counterpropagating waves [43, 49]. This interference between counterpropagating waves produces a standing wave. If the counterpart of this standing wave could be generated through some process, the cancellation of the Kerr nonreciprocity would be possible. A broadband light source, i.e., a low-coherence source, such

as superluminescent diodes (SLD) is one way for the Kerr effect compensation. Using MIOC square-wave modulation to bias the FOG for maximum signal-to-noise ratio by adding an optical gate at the output of the laser is a further method for eliminating the Kerr-induced drift [80].

Chapter 3

Numerical Studies

A conventional Panda-type PM fiber and a PM fiber with an elliptical core are the two most common designs of PM fiber, as illustrated in **Fig. 3.1a** I and II. The SAP in a typical Panda-type PM fiber (**Fig. 3.1a.I**) serve a crucial role in the sense that they extend all around the core, which causes the fiber core to be subjected to a significant amount of stress. SAPs are located in a typical Panda-type PM fiber, where polarized light propagates more slowly along the so-called slow axis. The axis orthogonal to the slow axis, along which light travels relatively at a faster velocity, is referred to as the fast axis. On the other hand, when polarized light is released along the major axis (slow axis) of the elliptical core of PM fiber (**Fig. 3.1a.II**), the light propagates at a slower velocity than if it was launched along the minor axis (fast axis). Therefore, we combined these two geometries providing as the design of biaxial PM fiber (P_x and P_y), as given in **Fig. 3.1a.III**. In this way, we anticipated that such PM fiber showing both a Panda-type and an elliptical core will possess the characteristics of these two designs.

In the case that the aforementioned geometries are combined, polarized light launched along the axis in which SAPs are positioned will be compelled to propagate at a slower velocity. When the polarized light is launched along the major axis of the elliptical core of PM fiber, however, then it will be forced to propagate relatively at a slower velocity through this axis, which is orthogonal to SAPs.

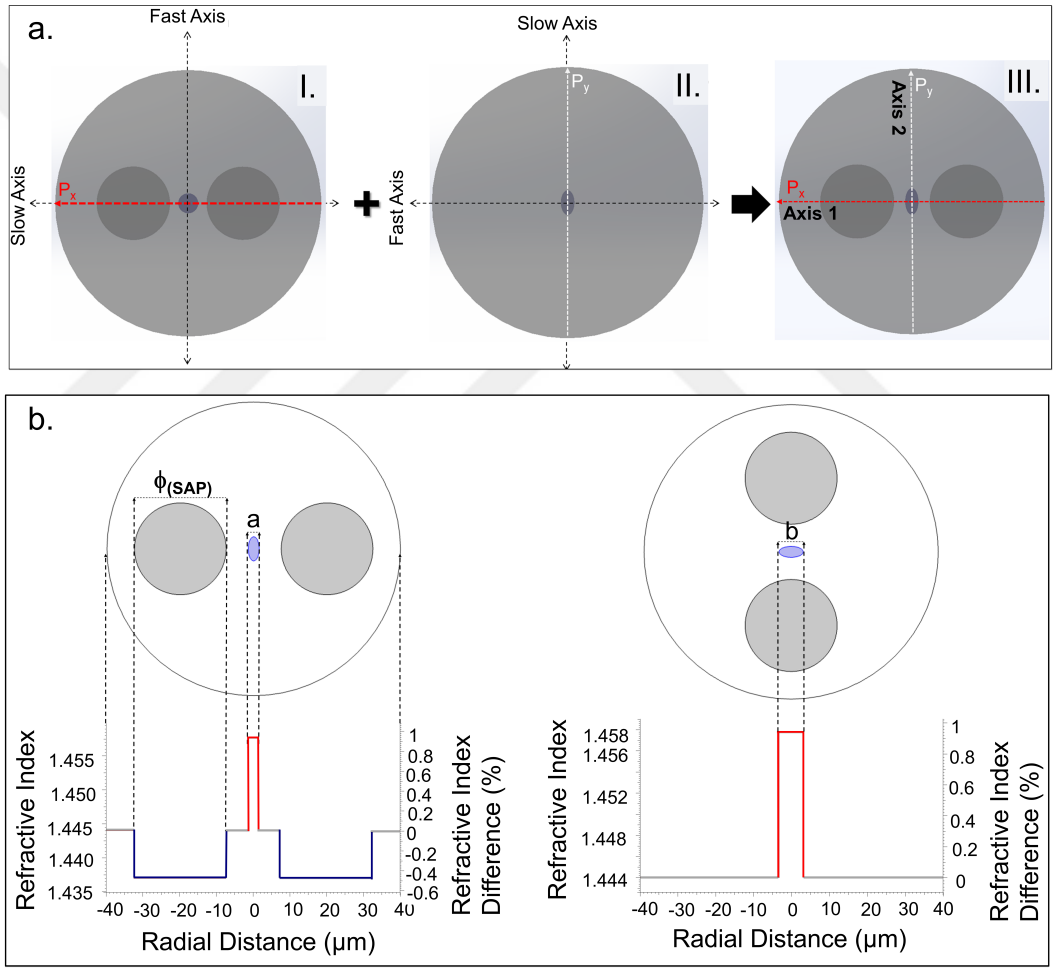

Figure 3.1: (a) The schematics of the biaxial PM fiber (III) formation by combining Panda-type (I) and elliptical core (II) PM fiber (b) the schematics of a cross-sectional image of the biaxial PM fiber with 80 μm cladding and the respective refractive index profiles along two axes

We performed the finite element method (FEM) using COMSOL to simulate the numerical studies. FEM is utilized to discretize the problem, divide it into smaller discrete parts (subdomains), named as elements, and thus have the geometrical model meshed, as presented in **Fig. 3.2**. In other words, this task of having a system or a structure relatively in much smaller pieces is often called meshing. However, several features and functionality, such as sequence type, element type, element order, element quality, specified size and distribution of elements, and mesh quality, should be taken into account during mesh building to ensure that the model geometry is properly and efficiently resolved for computation. Some important parameters used in numerical studies is also reported in **Table 3.1 and 2**.

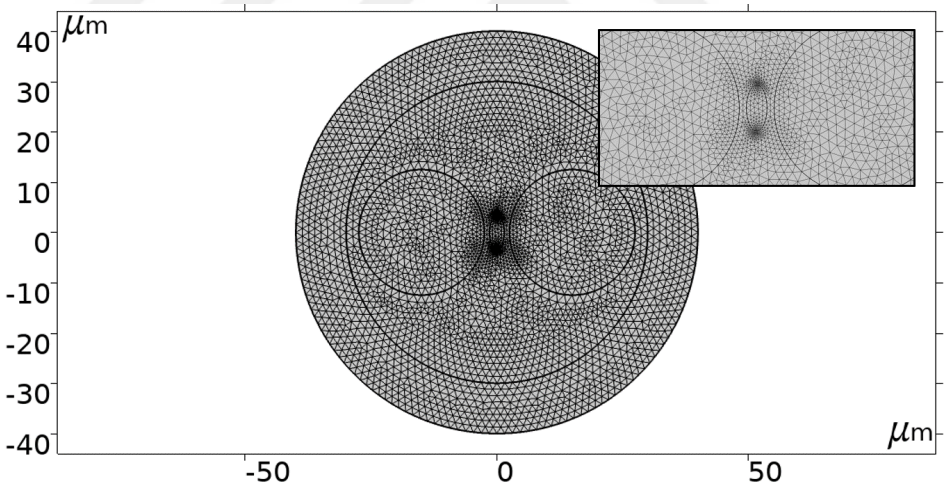

Figure 3.2: The representation of discretizing the model of proposed biaxial PM fiber into the finite shape of free triangular elements

The ellipticity of the biaxial PM fiber core is 0.6 which is determined using the equation expressed by,

$$\varepsilon = 1 - \frac{a}{b} \tag{3.1}$$

where a and b are values of the minor and major axes, respectively.

The initial biaxial PM fiber parameters, including a Hi-Bi Panda-type PM fiber design with a diameter of 25 μm of the SAPs that are highly doped B_2O_3, corresponding to a doping value of approximately 20 mol% were used for numerical simulations by taking the fiber optic gyroscope applications generally operating at a wavelength of 1550 nm into consideration. The cladding diameter of the biaxial PM fiber is 80 μm. The SAPs must be adequately separated from the core to reduce transmission loss. Furthermore, it is also required that SAPs must be as close to the core as possible to produce high birefringence [29]. Thus, the distance between the SAPs and the highly elliptical core was chosen as 6 μm. The region, where the fused silica buffer layer surrounds the SAPs, is sensitive to mechanical deformation under conditions of high-temperature drawing in a vacuum environment. As the region is subjected to drawing circumstances, its shape can be altered, especially in the direction of the fiber core. Therefore, we assumed that the strain is independent of the fiber cladding diameter along the z-direction. With this assumption, the diameter of the fiber, the tension of drawing, and temperature in the generalized plane strain formulation were maintained constant until the significantly elliptical core was detected during the manufacturing process. Since the polarization properties of Hi-Bi fibers are strongly sensitive to chemical composition, the trend of the refractive index (RI), which varies with different amounts of B_2O_3 into the SiO_2 glass network, and variations in the coefficient of thermal expansion (CTE) were studied well [81]. In the simulations for SAPs, a corresponding RI change of 7.9 x 10^{-3} and a CTE of 2.35 x 10^{-6} 1/K were applied. Moreover, an elliptical and a relatively high GeO_2-doped silica core of 5 mol% with an index difference around 1% (NA $\approx$ 0.20) were used to provide biaxial PM properties with Hi-Bi in **Fig. 3.1b**.

3.1 Hi-Bi Biaxial Panda Type Fiber Parameters and Modal Properties

Mechanical stress in optical fibers is a significant issue in fiber development and research since the intrinsic stress has an effect on the optical and mechanical properties of optical fibers and thus influences their modal behavior [10]. If this stress was sufficient to induce significant changes in the refractive index profiles of the different glass components (e.g. core and cladding) in the optical fiber, it became possible to create the optical anisotropy [82] that leads to birefringence. Therefore, we have investigated the effect of the lateral stress distribution using the finite-element method.

We applied the general linear stress-optical relation for PM fiber to calculate the stress-induced refractive index (RI) changes by using tensor notation [83], as follows:

$$\Delta n_{ij} = -B_{ijkl}\sigma_{kl} = n_{ij} - n_0 I_{ij} \tag{3.2}$$

where n_0 is the stress-free RI of the materials, I_{ij} is the identity tensor, B_{ijkl} is the stress-optical tensor, and σ_{kl} is the stress-tensor. As cylindrical symmetry is considered, the non-diagonal parts are not involved. Therefore, two independent stress-optical coefficients B_1 and B_2 as follows:

$$n_x = n_0 - B_1\sigma_x - B_2(\sigma_y + \sigma_z) \tag{3.3}$$

$$n_y = n_0 - B_1\sigma_y - B_2(\sigma_x + \sigma_z) \tag{3.4}$$

$$n_z = n_0 - B_1\sigma_z - B_2(\sigma_x + \sigma_y) \tag{3.5}$$

where B_1 and B_2 are inserted from [84] respectively 0.65 x 10^{-6} MPa^{-1} and 4.2 x 10^{-6} MPa^{-1}. The lateral stress distribution of the proposed PM fiber is represented in **Fig. 3.3a**. The biaxial modal birefringence is demonstrated in **Fig. 3.3b** as well. The modal birefringence along two orthogonal axes is found about 1.37 x 10^{-3} whose maximum and minimum values are 1.42 x 10^{-3} for Axis 1 and 1.16 x 10^{-3} for Axis 2 respectively, through the edges of the fiber core.

Table 3.1: The parameters used in numerical studies

n_{Si}	n_{SiO_2}	Δn	n_{Core}
3.5	1.444	0.0075	1.4575
ν_{Si}	ν_{SiO_2}	B_1 (1/Pa)	B_2 (1/Pa)
0.19	0.17	6.5 x 10^{-13}	4.2 x 10^{-12}
α_{Si} (1/K)	α_{SiO_2} (1/K)	E_{Si} (Pa)	E_{SiO_2} (Pa)
2.5 x 10^{-6}	3.5 x 10^{-7}	1.1 x 10^{11}	7.8 x 10^{10}
ρ_{Si} (kg/m^3)	ρ_{SiO_2} (kg/m^3)	T_0 (K)	T_1 (K)
2330	2203	2253.2	293.15

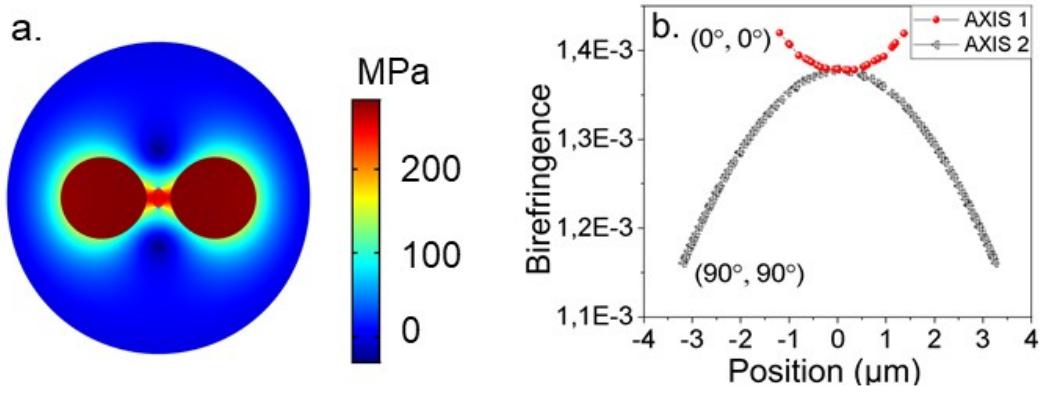

Figure 3.3: (a) The lateral stress distribution (b) the biaxial modal birefringence values of the proposed biaxial PM fiber.

Table 3.2: The MFDs and the difference of the propagation constants two axes

Launched Axis	MFD (μm)	$\Delta\beta$ (rad/m)
Axis 1	3.87	6.6 x 10^4
Axis 2	3.88	6.5 x 10^4

The change in the stress distributions along the edge of the fiber core causes the difference in the modal birefringence along two axes. The result of the modal birefringence, which was calculated in **Fig. 3.3b**, is greater than that of the majority of the typical all-glass-based PM fibers reported in [85]. The relation between modal birefringence and thickness of the stress-applying part, as reported in [12, 86] indicates that high modal birefringence values can be obtained till a diameter of $\varnothing_{SAP} \approx 60$ μm. Therefore, the further improvement in polarization extinction ratio (PER) values is enabled by considering that we possess the combination of conventional Panda-type PM fiber and elliptical core, including the SAPs with a diameter of $\varnothing_{SAP} \approx 25$ μm. Thus, it can be concluded that not only the maximum lateral stress level established in this study is greater compared to that represented in the preceding article [10] but also the biaxial birefringence values around two orders of magnitude are higher than the birefringence calculated [12].

The simulation results of the biaxial PM fiber parameters, such as the mode-field-distances (MFDs) and the propagation constant, are given in **Table 3.2** as the light is launched along two orthogonal axes.

In conclusion of the numerical results, it can be stated that the intrinsic stress generated by the proposed PM fiber design leads to a fairly significant variability difference between the propagation constants of two orthogonal polarized modes, ($\Delta\beta = \beta_{Axis1} - \beta_{Axis2}$) in rad/m, when the light is launched along Axis1. Moreover, the exhibited results indicate that the phase birefringence along the two axes is nearly identical with a minor difference along the fiber core's edges resulting from the fact that the stress increases along Axis1 or decreases along Axis2 in **Fig. 3.3b**.

Chapter 4

Fabrication of the Biaxial PM Fibers

The fiber preform with a diameter of 50 mm was obtained by the plasma-enhanced chemical vapor deposition (PCVD) fabrication process [87]. In order to have high birefringence in PM fibers, high doping concentration in the SARs, which were placed independently within two drilled holes in the preform, is required above 16% mole [9]. The finished preform was controlled for clarity, concentricity, and critical dimensions. High birefringence is particularly important in gyroscope applications where environmental conditions can degrade this property. Therefore, the performance of PM fibers under such environmental conditions including temperature changes must be tested.

In order to have drawing conditions, a dummy preform with the same geometry of the real PM fiber preform was utilized. The drawing parameters, such as fiber drawing temperature and speed, preform feed speed, primary and secondary polymer pressure and temperature, and the sizes of coating dyes were determined. High-temperature fiber drawing tower (**Fig. 4.1**) was aligned one day before the real drawing, pre-determined dyes were inserted into the fiber drawing tower, and the polymer tanks were heated to 30 °C. In the day of drawing the PM fiber, the preform was also aligned with respect to the center of the high-temperature

Figure 4.1: High-temperature fiber drawing tower

furnace. High-temperature fiber drawing was started when the preform tip at the center of the heating zone was melted and dropped via the gravitation through the end of the furnace and the first capstan. When the capstan was closed, the diameter of the first drop was decreased to the requested size of the PM fiber cladding around 80 μm. After this point, the fiber was fed downstairs where the polymer coating units were present. After the insertion of the PM fiber through coating units and the second capstan, the first capstan was closed. And then, the primary and the secondary polymer coating processes were started. The fiber diameter was kept at the target diameter of 80 μm during the fiber drawing process. At the end of the process, the entire fiber was coated with double UV-acrylic polymers to provide mechanical protection and maximize fiber strength.

The biaxial PM fibers with a length of over 3 km were drawn under a vacuum at 1 mBar. Throughout the fiber drawing process, a near-infrared pyrometer with a sensitivity of 15 °C was used to control and measure the temperature. The core of the fiber was formed as a circular, elliptical, and highly elliptical core by adjusting the temperature as T_1 = 1950 °C, T_2 = 1970 °C, and T_3 = 1990 °C respectively in the initial part of the drawing, as illustrated in **Fig. 4.2**. This indicates that the shape of the PM fiber core can be changed and controlled by applying different temperatures while all other drawing parameters (drawing speed of 15 m/min, etc.) are maintained constant.

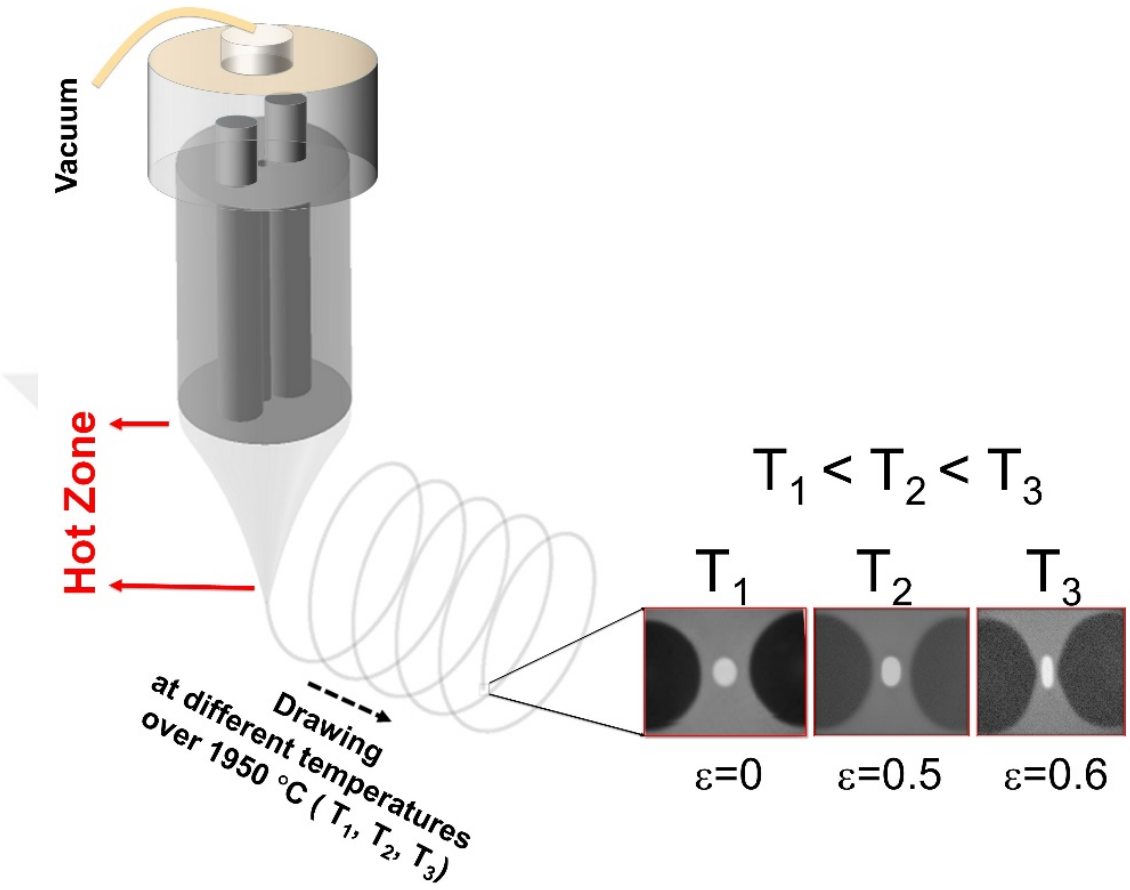

Figure 4.2: Schematic of the biaxial PM fiber drawing at different temperatures over 1950 °C demonstrates its controlled formation

The backscattered SEM image of PM fiber was obtained to determine the exact sizes of the core along minor and major axes and SAPs, as presented in **Fig. 4.3b**. The combination of a Panda-type PM fiber and an elliptical core PM fiber was manufactured as a novel geometry with a cladding diameter of 80 μm. Along the orthogonal axis (Axis 2) to the axis (Axis 1), where the stress-applying parts (SAPs) are placed, the ellipticity with a length of 6.3 μm and 2.8 μm along minor and major axes, respectively, was generated. The core, SAPs, and cladding differ by brightness due to variations in elemental distributions such as Ge-doped core, B-doped SAPs, and pure SiO_2 cladding, respectively. Wavelength dispersive X-ray spectroscopy (WDS) measurements confirmed these differences, including 5 mol% GeO_2-doped silica along the core and 20 mol% B_2O_3-doped silica along the SAPs.

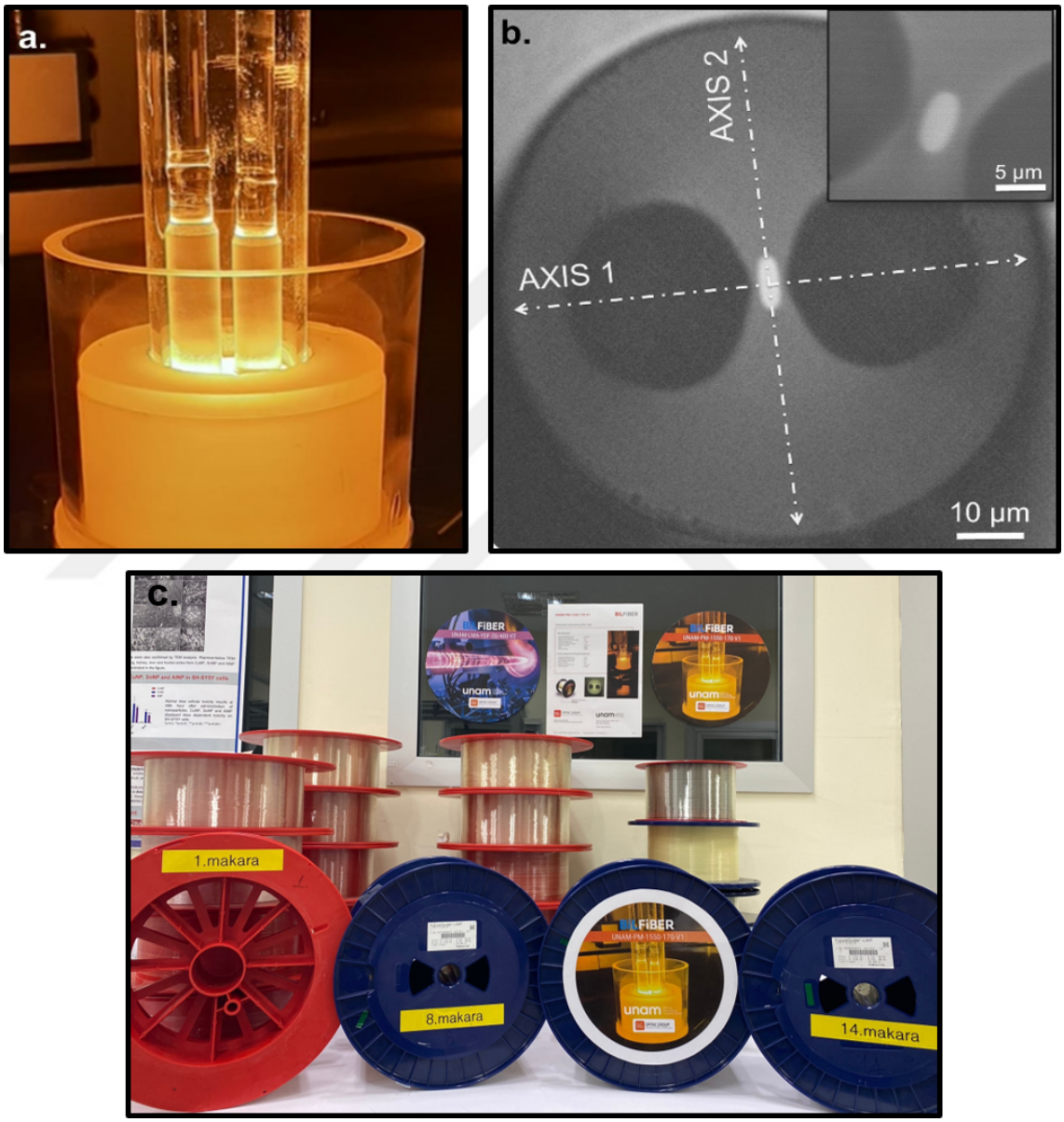

Figure 4.3: (a) An image of the PM fiber preform when conducting the biaxial PM fiber drawing (b) the cross-sectional optical image of 3 km end face of the biaxial PM fiber with 80 μm cladding. In the inset, a back-scattered SEM image is provided (c) The entire production of the biaxial Hi-Bi PM fiber coils with a length of 100 km

Chapter 5

Characterization and Performance Tests

Once the cladding diameter stabilized at 80 μm $\pm$ 1 μm during the fiber preform drawing, we began to use an optical microscope (Model: Zeiss Axio) to scan the structural changes during the drawing process. After the drawing process was completed, a length of fiber was taken as a sample and cleaved by an optical fiber cleaver (Model: Fujikura CT105+) and the fiber's cross-section was coated with a 10 nm Au-Pd coating before collecting scanning electron microscope (SEM) images. Then, the back-scattered SEM images, as given in **Fig. 4.2b**, were collected using a high-resolution SEM (Model: FEI NanoSEM) at 20 kV potential. The wavelength dispersive X-ray spectroscopy (WDS) measurements were also performed utilizing a spectrometer (Model: Oxford Instruments), which was mounted within the SEM.

With the use of two-point bending measurements (Model: FiberSigma) and a micromechanical tester (Model: Instron 5900 Series), the mechanical characteristics, such as the minimum diameter and the fiber breaking point, of the biaxial PM fiber were determined to demonstrate the fiber's performance. The results are listed in **Table 5.1** and they are compatible with the typical Hi-Bi PM fibers.

Table 5.1: The mechanical properties of the biaxial PM fiber

Biaxial PM Fiber	
Two-point Bending Measurement	< 1.5 mm (no breaking occurred)
Micromechanical Tester (Breaking Force)	3.9 ± 0.2 GN/m^2 (≈ 565 kpsi)

In measurements of two-point bending, the instrument's minimum bending diameter is 1.5 mm, and the biaxial PM fiber was not broken until this point. On the other hand, during the tensile test, the fiber is stretched from both sides. The breaking force is measured as the fiber was completely broken from the center of the tested fiber. These measurements have been conducted a minimum of three times.

The optical time-domain reflectometer (OTDR) (Model: AFL FLEXSCAN) measurement was performed for the determination of the optical loss, as given in **Fig. 5.1**. The measurement indicates that the optical loss at the wavelength of 1550 nm is approximately 1.42 $\pm$ 0.08 dB/km, with a homogeneity over 3 km length, which can be considered to be compatible with the commercial fibers fabricated by Coherent/Nufern (Product: PM1550G-80/170-5) [88] and Corning (Product: RC PM 1550) [89], as tabulated in **Table: A.1**.

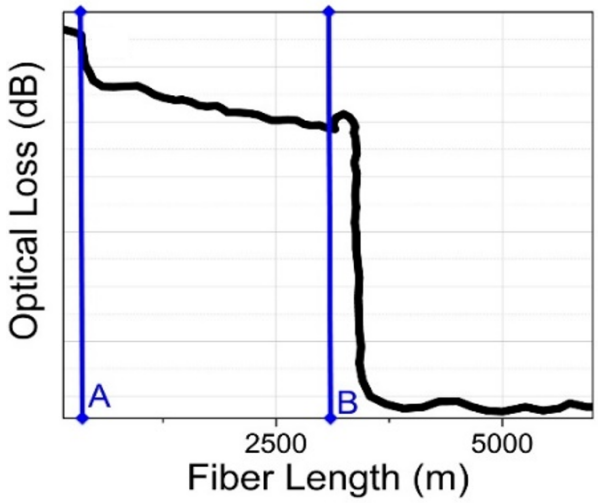

Figure 5.1: The OTDR measurement for the determination of the optical loss at 1550 nm along over 3 km length between the points A and B

Moreover, the NAs and the MFDs of the output polarized light along two axes were determined by spatially recording the light intensity distribution at different angles, as given in **Fig. 5.2**, employing a conventional technique known as direct far-field scan [90]. The measurements were performed separately for the fast and slow axes of the biaxial PM fiber. It is very important to ensure that the center of the photodetector's detection area is located directly opposite the fiber end at 0°. The angle of scanning was increased until the photodetector read no light intensity.

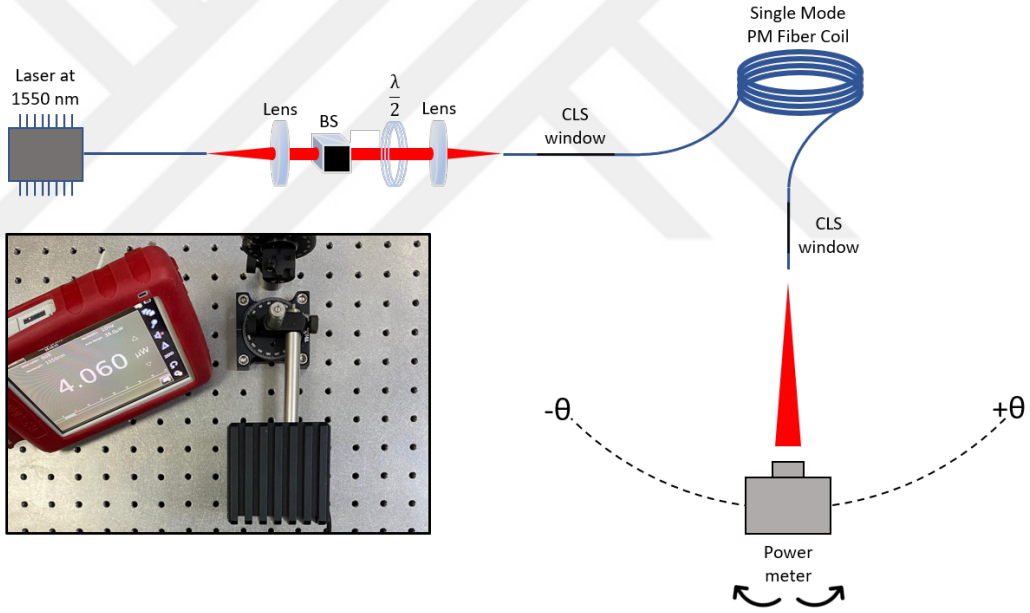

Figure 5.2: The optical setup configuration to determine the NAs and MFDs of the test biaxial PM fiber

The $sin\theta$ values were calculated, as shown in **Fig. 5.3**, for the determination of NA values along two PM axes and also outlined in **Table 5.2**.

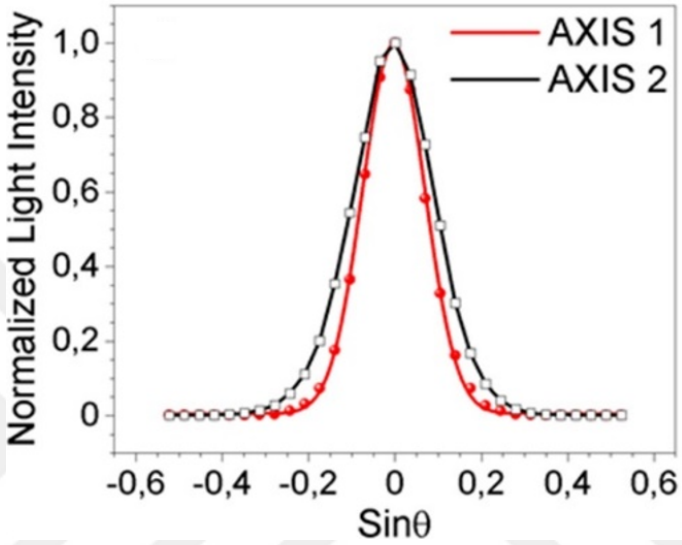

Figure 5.3: Normalized light intensity collected at the output of the biaxial PM fiber at various angles for the determination of its NAs and MFDs in two different incident light launch conditions along Axis 1 and Axis 2.

Moreover, the Petermann II formulization [91, 92], which is referred to as a ratio of integrals from the far-field intensity distribution, is utilized as follows:

$$MFD = \frac{\lambda\sqrt{2}}{\pi}\left[\frac{\int_0^{\frac{\pi}{2}} P_F(\theta)\sin\theta\cos\theta d\theta)}{\int_0^{\frac{\pi}{2}} P_F(\theta)\sin^3\theta\cos\theta d\theta}\right]^{\frac{1}{2}} \tag{5.1}$$

where $P_F(\theta)$ is the far-field intensity distribution, λ is the wavelength in μm and θ is the angle in the far-field measurement from the axis of the fiber. The MFD values, as reported in **Table 5.2**, were determined to be close to the experimental error ($\pm$ 0.5 μm) of the numerical studies' results.

The characterization of step-index single-mode PM fiber was also examined by considering the relation between V-number and cut-off wavelength expressed by,

$$V = \frac{2\pi a}{\lambda} sin\theta = \frac{2\pi a}{\lambda} NA \tag{5.2}$$

$$\lambda_c^{th} = \frac{2\pi a}{V} NA \tag{5.3}$$

where a is the mode field radius. The cut-off wavelengths for each axis (Axis 1 and Axis 2) were determined using the MFD and NA values from **Table 5.2** and presented in **Fig. 5.4**. The cut-off wavelengths were measured at about 1028.5 nm for Axis 1 and 995.5 nm for Axis 2. At these and longer wavelengths, our proposed biaxial PM fiber behaves as a single-mode fiber since only the fundamental mode propagates through it.

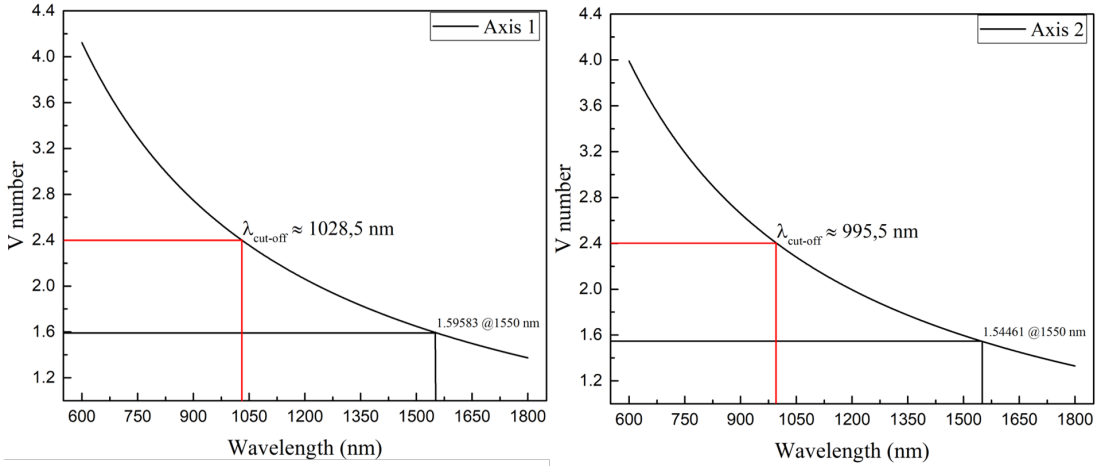

Figure 5.4: The cut-off wavelengths of PMF for Axis 1 and Axis 2

For the measurement of the polarization extinction ratio (PER), the in-house built set-up was performed, as shown in **Fig. 5.5**. An incident 35 dB polarized light launched from a laser source was coupled to the core of the test biaxial PM fiber in between two polarizing beam splitters with the help of optical components given in the schematic. Cladding light stripper (CLS) components were also implemented at both ends of the test biaxial PM fiber. In this way, the unwanted residual pump power is removed from the system [93].

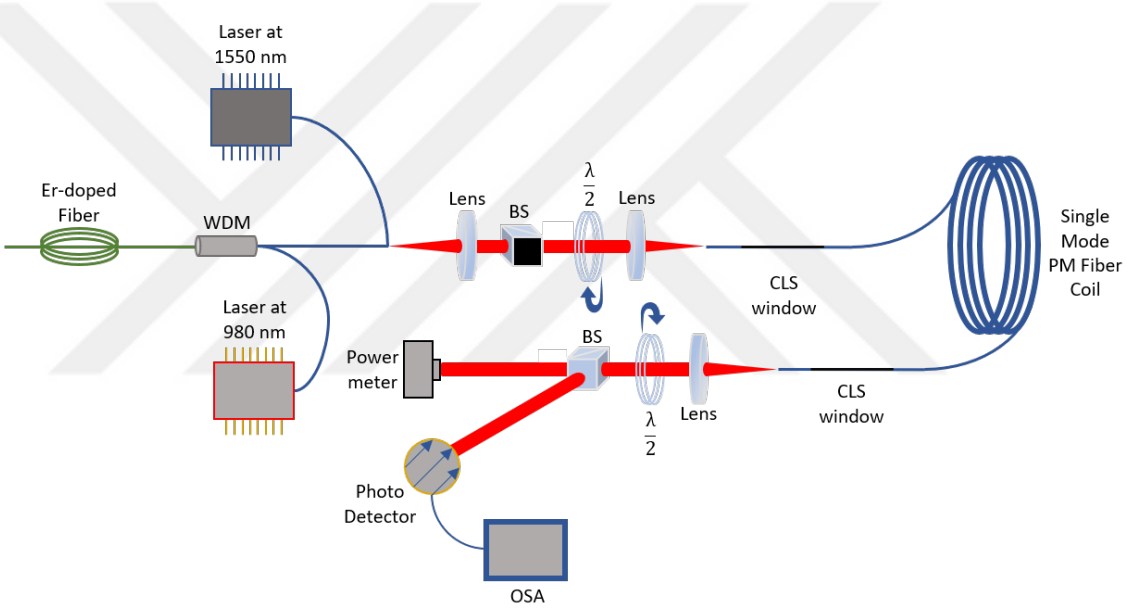

Figure 5.5: The optical setup configuration of PM fiber characterization

The x-and y-mode polarization modes, as illustrated in **Fig. 5.6**, at the entrance and exit of the fiber could be selected by using a pair of half-wave plates, which serve as polarizers and analyzers, and polarization beam splitters. A power meter (Model: Coherent FieldMax II) was also utilized to measure the power values of each polarized beam. Therefore, the light, which is coupled to the PM fiber and propagates through the test biaxial PM fiber, is said to determine to what extent the polarization of the light is maintained.

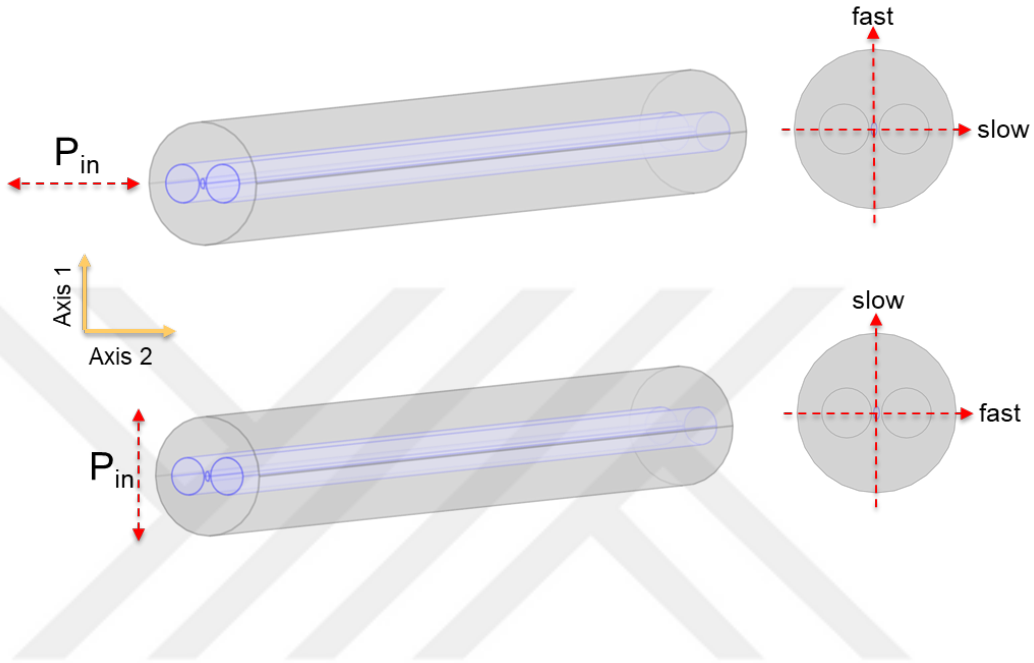

Figure 5.6: Launching light with linear polarization (≈35 dB) along parallel (Axis 1) and perpendicular (Axis 2) to SAPs conducted in the PER measurements

With the use of a 980/1550 nm wavelength division multiplexer (WDM) with HI1060 fiber connectors, we pumped 1.5 m of an Er-doped fiber (Model: Liekki Er80-8/125) to generate a back-scattered amplified spontaneous emission (ASE) source. At the other end of the WDM, the ASE was launched through the test biaxial PM fiber for the interference spectra, which were collected by using an optical spectrum analyzer (OSA), as presented in **Fig. 5.5**, along two polarization-maintaining axes. The high PM property is provided for both axes (Axis 1 and Axis 2) due to the novel combination of Panda-type and elliptical core PM fiber. As the SAPs enable PM property along the axis (Axis 1), which is conventionally called the slow-axis, Axis 2 possesses an additional high PM property created by the elliptical core geometry when the light is launched along this axis.

In order to verify the accuracy of the numerical results, the PER measurements were first carried out independently along these two axes at room temperature. The PER values of the test biaxial PM fiber length of 110 m along Axis 1 and Axis 2 are given in **Fig. 5.7a**, and **Table 5.2** provides the experimental results along two axes that validate the biaxial PM properties of greater than 30 dB along both axes. Our results were observed to be compatible with the commercial fibers manufactured by the companies such as, Coherent/Nufern (Product No: PM1550G-80/135-2HP and PM1550G-80/170-5) [88], Corning (Product No: RC PM 1550) [89], and YOFC (Product No: PM1550 80-18/135) [94].

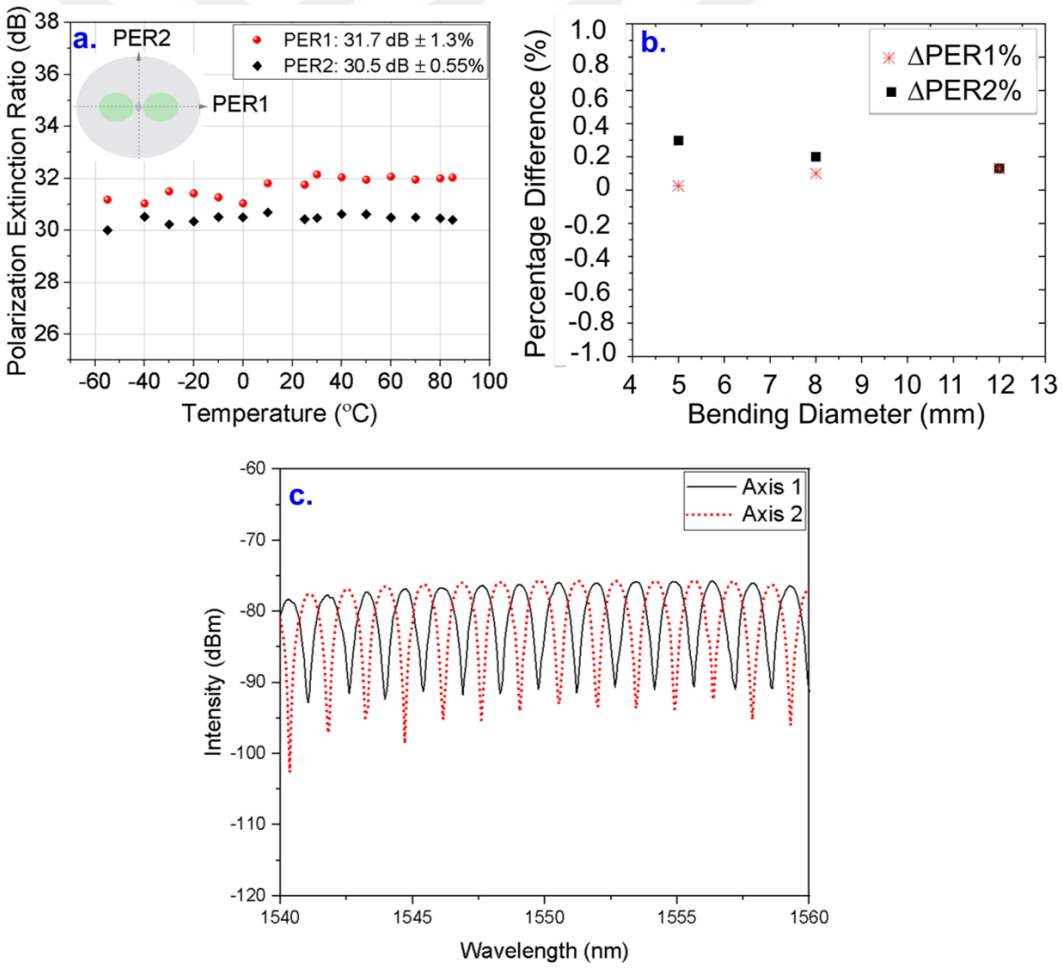

Figure 5.7: (a) The PER measurements at different operating temperatures from -55 °C to +85 °C (b) The bending diameter dependent PER deterioration along two axes (c) The interference spectra of the biaxial PM fiber as a function of wavelength with the polarizations oriented at 45° to the polarization axes Axis 1 and Axis 2

Table 5.2: The experimental modal properties at the wavelength of around 1550 nm

Biaxial PMF	NA	MFD (μm)	PER (dB)	$B_{L(Group)}$ (mm)	B_{Group}
Axis 1	0.181	4.35	31.7 ± 1.3%	1.40	(1.12 ± 0.33) x 10^{-3}
Axis 2	0.176	4.33	30.5 ± 0.5%	1.45	(1.07 ± 0.32) x 10^{-3}

The PER measurements were not just completed in a room temperature environment. They were also conducted in harsh temperature conditions, where the differences in the PM property between Axis 1 and Axis 2 are ±0.5 % and ±1.3 % approximately, respectively. Firstly, the test biaxial PM fiber was placed inside a furnace (Model: NUVE EVO18) to conduct the PM properties at temperatures from 25 °C to 85 °C. Secondly, the PM properties were examined in a container filled with liquid nitrogen at temperatures ranging from 25 °C to -55 °C while the thermocouple continuously measured the temperature. We kept the fiber sample for several hours at these temperatures and at a storage temperature of -20 °C for over a day. Eventually, there was almost no degradation observed in the PER values along both axes. Besides, fiber optic based sensors [95], particularly PM-fiber optic based sensors [96], are commonly employed for environmental monitoring, in which the fiber is exposed to a wide range of temperatures. Moreover, at three different bending diameters (⌀ = 5, 8, and 12 mm), the bending performance of biaxial PM fiber was tested in terms of loss in the PERs along two axes. As the **Fig. 5.7b** demonstrates, the maximum loss in the PERs along two axes is less than 0.5 % for all bending diameters examined.

The PER measurements were also conducted in order to investigate the impact of drawing conditions on the geometry and PER performance of the biaxial PM fibers, as presented in **Fig. 5.8** and the results are tabulated in **Table 5.3**. As the different temperatures (T_1= 1950 °C, T_2= 1970 °C, and T_3= 1990 °C) were adjusted to fiber preform during the initial part of the drawing process, the core of the fiber was formed as a circular, elliptical, and highly elliptical core. In this way, it is concluded that the shape of the PM fiber core can be changed

Table 5.3: The PER values of PM fiber for both axes with different ellipticities of core radius

Biaxial PM Fiber	PER (dB)	Distance between SAPs (μm)
ε= 0.12	28.5	10.86
ε= 0.40	30.5	8.83
ε= 0.50	31.7	6.57

and controlled. Conditions for the formation of the Hi-Bi biaxial PM fiber were obtained. These temperature variations not only resulted in structural changes to the fiber core but also influenced PER measurements. As the temperature increases, the boron-doped rods approach each other, and the fiber core becomes gradually elliptical. The reduction in the distance between the rods causes a higher intrinsic pressure on the axis due to the stress created on the fiber core, thus yielding the Hi-Bi property and the PER values over two principal axes **Fig. 5.7**.

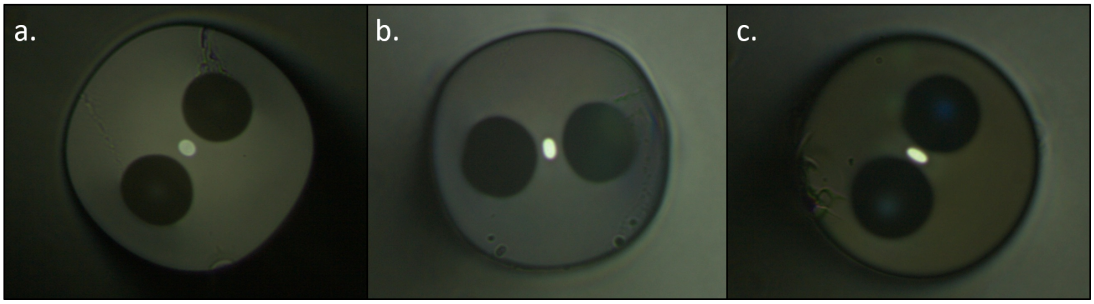

Figure 5.8: (a) The cross-section of PM fiber with an ellipticity of ε= 0.12, (b) ε= 0.40, and (c) ε= 0.50, respectively

The second method for validating the biaxial PM property involves measuring the beat length values at the polarizations oriented with 45° angles to the main polarized axis. The **Fig. 5.7c** shows the interference spectra of the biaxial PM fiber when the amplified spontaneous emission (ASE) source was launched at 45° to Axis 1 and Axis 2. In this way, it enables to collect the broadband interference pattern between the respective slow and fast axes for each polarization-maintaining axis that become in and out of phase together. When light is launched at the polarizations oriented with 45° angles to the major axis of

the elliptical core, the same technique is applied to the determination of the beat length. Therefore, there occurs $\pi/2$ difference in angles between launched axes to determine the beat length for Axis 1 and Axis 2. Thus, $\Delta\lambda$ values corresponding to the distance between two consecutive peaks at about 1550 nm were measured. Then, group beat length is calculated over a particular length of the biaxial fiber in the following manner [2]:

$$B_{L(Group)}(mm) = \frac{(\Delta\lambda)L}{\lambda} \tag{5.4}$$

Then, the group birefringence values for each polarization-maintaining axis were found as follows:

$$B_{(Group)} = \frac{\lambda^2}{(\Delta\lambda)L} = \frac{\lambda}{B_{L(Group)}} \tag{5.5}$$

As the results along two axes are reported in **Table 5.2**, the corresponding group beat length and the group birefringence values are below 1.5 mm and around 1.1 x 10^{-3} with a standard deviation of ± 0.33 and ± 0.32, respectively.

As the difference between phase birefringence and group birefringence of PMFs is theoretically and experimentally discussed in [97], these differences depend on the design of the PM fibers. In the shape-induced birefringence PM fibers, such as the case in elliptical-core fibers, the group and phase birefringence values are different, and even the group birefringence can be as twice as the phase birefringence. Beside, the two birefringences of the stress-induced birefringence PM fibers are nearly identical, as in Panda-type PM fibers. On the other hand, both stress-induced birefringence and geometry-induced birefringence are present in the biaxial PM fiber examined in this study. It can be stated that the group birefringence is one to two times greater than the phase birefringence.

5.1 Tapering Effect on Hi-Bi PM Fiber

The term "taper" refers to the gradual increase or decrease in fiber core diameter along the length of the fiber [2]. In this section, the method of taper drawing is employed to fabricate the microscopic optical fibers with extraordinary diameter uniformities. To produce the tapered devices, an arc fusion splicer (Model: Fujikura FSM-100M+) was utilized. As it is illustrated in **Fig. 5.9**, a section of the fiber was heated and stretched into different cladding diameters (around 45, 31, and 16 μm), as shown in **Fig. 5.10**, by taking care the transition is adiabatic as much as possible, to ensure that the test biaxial PM fiber still preserves its optical properties and the input polarization state of the propagating signal at the fiber output.

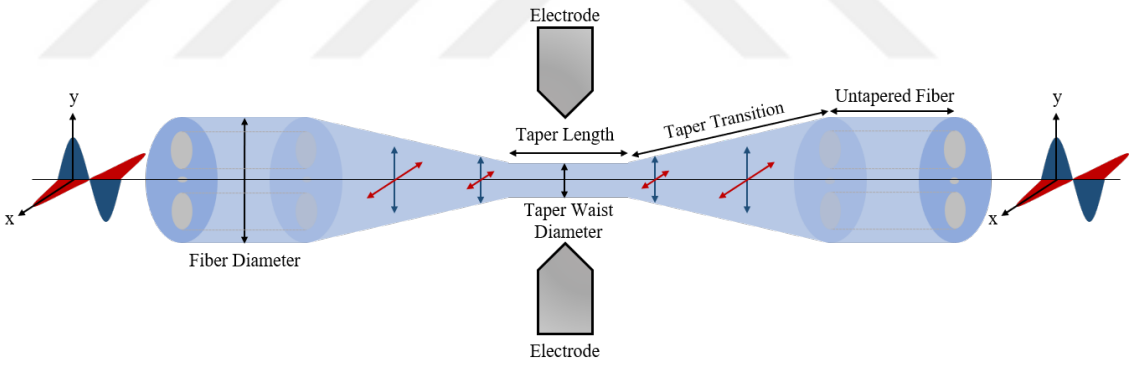

Figure 5.9: Schematic diagram of an adiabatically tapered PM fiber

The polarization-extinction ratio (PER) measurements were observed for each axes (Axis1 and Axis2) at different taper waist diameters, as summarized in **Table 5.4**. The PER measurements were repeated two times at different angles θ_1 and θ_2, with an angle difference of 90° difference between them. As the angle was chosen where the PER value is highest, the beat length measurements were obtained for each different waist diameter, in **Fig. 5.11**. After the tapering process, it is evident that PER values decreased from over 30 dB, which corresponds to the degree of polarization (DoP) of 99.9 %. However, even with the minimum taper waist diameter (around 16.5 μm), the PER values vary from 16 dB (DoP: 97.5 %) to 19 dB (DoP: 98.7 %) which is considered acceptable in the majority

of instances according to [98].

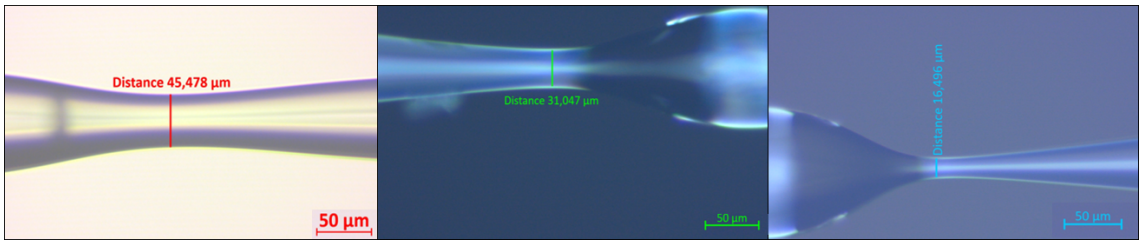

Figure 5.10: The optical microscope images of the tapered PM fibers with different waist diameters (a) around 45.5 μm, (b) 31 μm, and (c) 16.5 μm, respectively

Table 5.4: The PER values of the tapered PM fibers with different waist diameters

	Axis 1		Axis 2	
Waist Diameter (μm)	$PER_{\theta 1}$ (dB)	$PER_{\theta 2}$ (dB)	$PER_{\theta 1}$ (dB)	$PER_{\theta 2}$ (dB)
45.5	16.10	16.00	16.09	16.16
31.0	16.92	16.97	17.03	16.85
16.5	18.98	17.83	19.18	17.85

Although the beat length values increased and the birefringence values decreased by 23 % respectively in the case of tapered biaxial PM fiber, resulted in **Table 5.5**, compared to the untapered case, resulted in **Table 5.2**, these values are observed to be superior to that found in the previous reports [5, 99]. Therefore, one can conclude that the biaxial PM property is still validated under the tapered condition.

Table 5.5: The beat length and birefringence values of the tapered biaxial PM fiber with taper waist diameters

Taper Waist Diameter (μm)	Beat Length (mm)	Birefringence
45.5	1.873	8.25×10^{-4}
31.0	1.843	8.41×10^{-4}
16.5	1.806	8.58×10^{-4}

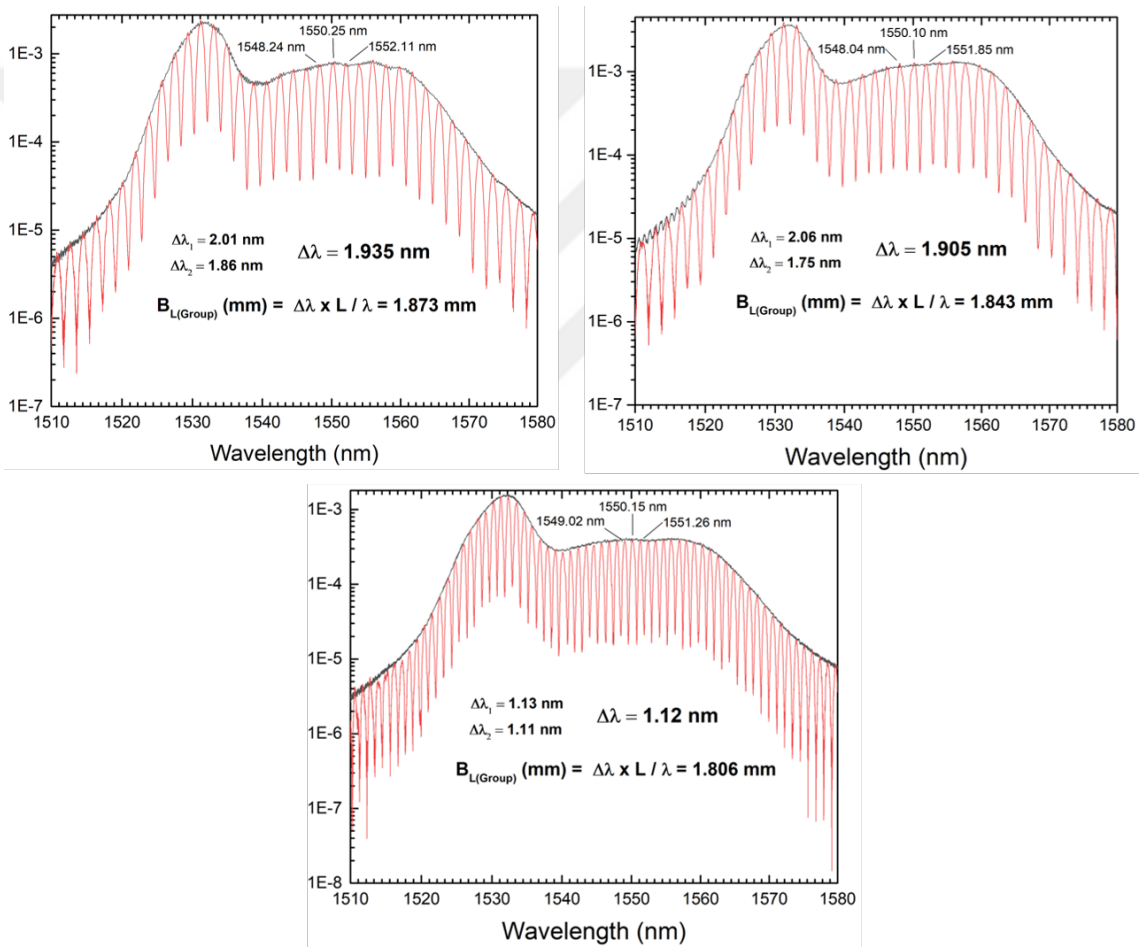

Figure 5.11: The beat length measurements of the tapered fibers (a) around 45.5 mm, (b) 31 mm, and (c) 16.5 mm, respectively

Chapter 6

Conclusion

In this study, the fiber preform with a diameter of 50 mm was produced by the modified chemical vapor deposition (MCVD) fabrication process and the symmetrical boron-doped stress-applying rods (SARs) were placed independently within two drilled holes in the preform. A Hi-Bi biaxial PM fiber was fabricated by adjusting the different temperatures in order to form circular, elliptical, and highly elliptical core during the fiber preform drawing. This unique manufacturing method has been discovered to contribute to the creation of such Hi-Bi fibers by reducing the distance between the SAPs and the core. Therefore, the biaxial PM fibers with a length of over 3 km were fabricated from the fiber preform. Also, the biaxial PM feature was confirmed by finite element method studies using COMSOL. The numerical studies of the initial biaxial PM fiber parameters were formed by taking the gyroscope applications generally operated at 1550 nm into account, including a Hi-Bi PM fiber with Panda-type PM fiber design, the SAPs with a diameter of 25 μm, and 5 mol% GeO_2-doped silica along the core and 20 mol% B_2O_3-doped silica along the SAPs. An optical microscope, a scanning electron microscope (SEM), a wavelength dispersive X-ray spectroscopy (WDS), two-point bending equipment, an optical time-domain reflectometer (OTDR), and an optical spectrum analyzer (OSA) were the leading main characterization tools that have been used. A fiber length of 110 m was tested for the determination of PER studies. PER values of our biaxial PM fiber were greater than 30

dB along two axes at different harsh operating temperatures from -55 °C to +85 °C. Along two polarized axes, the mode field diameter (MFD) and the numerical aperture (NA) values were also determined. Moreover, PER-supporting group beat length measurements indicated high birefringence values along two PM axes. The production of the Hi-Bi biaxial PM fiber with an elliptical core perpendicular to the SAPs necessitates two primary criteria, which were (i) a comparatively high level of B_2O_3 doping in the SAPs and (ii) a significantly higher drawing temperature compared to the conventional Panda-type PM fibers. We achieved less than 1.5 dB/km of optical loss over a distance of 3 kilometers, with excellent uniformity. Furthermore, t he results of the micromechanical testing and the 2-point bending measurement techniques indicated that the Hi-Bi biaxial PM fiber possesses a mechanical property that is consistent with that of conventional PM fibers. Moreover, the different waist diameters of the tapered elliptical core Panda-type PM fiber were manufactured with the taper drawing technique, using an arc fusion splicer. For each waist diameter, the beat length and birefringence measurements were obtained and observed to be superior to that found in the other studies. The biaxial PM property, therefore, was still proven even under the tapered condition. To conclude, this novel PM fiber type can be integrated into fiber optic systems that use either elliptical core or Panda-type PM fibers with minimal loss, and high polarization maintenance.

Bibliography

[1] T. L. Singal, *Optical fiber communications: principles and applications*. Cambridge University Press, 2016.

[2] A. Méndez and T. F. Morse, *Specialty optical fibers handbook*. Elsevier, 2011.

[3] W. Tong, H. Wang, J. Luo, and D. Liu, "Fabrication of a long-length and low-loss pmf and measurement of its properties," in *Passive Components and Fiber-based Devices II*, vol. 6019, pp. 120–124, SPIE, 2005.

[4] D. Goff, *Fiber optic reference guide*. Routledge, 2002.

[5] H. Li, X. Li, J. Wang, M. Rochette, and H. Yang, "High extinction ratio elliptical core panda-type polarization-maintaining fiber coil," *Optics Letters*, vol. 46, no. 17, pp. 4276–4279, 2021.

[6] P. Zhou, L. Huang, J. Xu, P. Ma, R. Su, J. Wu, and Z. Liu, "High power linearly polarized fiber laser: Generation, manipulation and application," *Science China Technological Sciences*, vol. 60, no. 12, pp. 1784–1800, 2017.

[7] Z. Ding, C.-P. Liang, and Y. Chen, "Technology developments and biomedical applications of polarization-sensitive optical coherence tomography," *Frontiers of Optoelectronics*, vol. 8, no. 2, pp. 128–140, 2015.

[8] J.-i. Sakai and T. Kimura, "Birefringence and polarization characteristics of single-mode optical fibers under elastic deformations," *IEEE Journal of Quantum Electronics*, vol. 17, no. 6, pp. 1041–1051, 1981.

[9] A. Karatutlu, E. Y. Yıldırım, E. Kendir, Y. Midilli, S. Akçimen, and B. Ortaç, "Fabrication of biaxial polarization-maintaining optical fiber with ultra-low bending-dependent polarization extinction ratio deterioration," *Optical Fiber Technology*, vol. 69, p. 102836, 2022.

[10] F. Just, R. Spittel, J. Bierlich, S. Grimm, M. Jäger, and H. Bartelt, "The influence of the fiber drawing process on intrinsic stress and the resulting birefringence optimization of pm fibers," *Optical Materials*, vol. 42, pp. 345–350, 2015.

[11] C. Emslie, "Polarization maintaining," *Specialty Optical Fibers Handbook*, p. 243, 2011.

[12] J. Noda, K. Okamoto, and Y. Sasaki, "Polarization-maintaining fibers and their applications," *Journal of Lightwave Technology*, vol. 4, no. 8, pp. 1071–1089, 1986.

[13] J. Laferrière, G. Lietaert, R. Taws, and S. Wolszczok, *Reference guide to fiber optic testing*, vol. 1. JDS Uniphase Corporation San Jose, CA, USA, 2007.

[14] N. I. Zanoon, "The phenomenon of total internal reflection and acceleration of light in fiber optics," *International Journal of Computer Applications*, vol. 975, p. 8887, 2014.

[15] C.-A. Bunge, M. Beckers, and T. Gries, *Polymer Optical Fibres: Fibre Types, Materials, Fabrication, Characterisation and Applications*. Woodhead Publishing, 2016.

[16] J. W. Shirley, "An early experimental determination of snell's law," *American Journal of Physics*, vol. 19, no. 9, pp. 507–508, 1951.

[17] M. Born and E. Wolf, *Principles of optics: electromagnetic theory of propagation, interference and diffraction of light*. Elsevier, 2013.

[18] D. Drosdoff and A. Widom, "Snell's law from an elementary particle viewpoint," *American journal of physics*, vol. 73, no. 10, pp. 973–975, 2005.

[19] J. Metz, "The geometry of snell's law," *The Physics Teacher*, vol. 52, no. 3, pp. 177–177, 2014.

[20] P. Chakrabarti, *Optical Fiber Communication*. McGraw-Hill Education, 2015.

[21] R. J. Potter, "Transmission properties of optical fibers," *JOSA*, vol. 51, no. 10, pp. 1079–1089, 1961.

[22] N. A. Issa and W. E. Padden, "Light acceptance properties of multimode microstructured optical fibers: Impact of multiple layers," *Optics Express*, vol. 12, no. 14, pp. 3224–3235, 2004.

[23] R. Nasirifar, M. Danaie, and A. Dideban, "Hollow-core graded index optical fiber refractive index sensor based on surface plasmon resonance," *Optical and Quantum Electronics*, vol. 52, no. 7, pp. 1–23, 2020.

[24] Y. Kato, K. Kitayama, S. Seikai, and N. Uchida, "Effective cutoff wavelength of the lp 11 mode in single-mode fiber cables," *IEEE Journal of Quantum Electronics*, vol. 17, no. 1, pp. 35–39, 1981.

[25] O. Çelikel, "Mode field diameter and cut-off wavelength measurements of single mode optical fiber standards used in otdr calibrations," *Optical and quantum electronics*, vol. 37, no. 6, pp. 587–604, 2005.

[26] D. Bayuwati, T. Waluyo, and I. Mulyanto, "Determination of the effective cut-off wavelength of several single-mode fiber patchcords," in *Journal of Physics: Conference Series*, vol. 985, p. 012002, IOP Publishing, 2018.

[27] A. A. GHATAK, A. Ghatak, K. Thyagarajan, and K. Thyagarajan, *An introduction to fiber optics*. Cambridge university press, 1998.

[28] L. Wang and S. LaRochelle, "Design of eight-mode polarization-maintaining few-mode fiber for multiple-input multiple-output-free spatial division multiplexing," *Optics letters*, vol. 40, no. 24, pp. 5846–5849, 2015.

[29] N. Shibata, Y. Sasaki, K. Okamoto, and T. Hosaka, "Fabrication of polarization-maintaining and absorption-reducing fibers," *Journal of Lightwave Technology*, vol. 1, no. 1, pp. 38–43, 1983.

[30] L. J. Vandergriff and V. McLean, "Nature and properties of light," *Fundamentals of Photonics*, pp. 1–38, 2008.

[31] J. Shipman, J. D. Wilson, C. A. Higgins, and B. Lou, *An introduction to physical science*. Cengage Learning, 2020.

[32] W. L. Stutzman, *Polarization in electromagnetic systems*. Artech house, 2018.

[33] M. Avadhanulu, *A textbook of engineering physics*. S. Chand Publishing, 2008.

[34] D. Singh, *Fundamentals of optics*. PHI Learning Pvt. Ltd., 2015.

[35] G. Konnen and G. Können, *Polarized light in nature*. CUP Archive, 1985.

[36] S. Rashleigh, "Origins and control of polarization effects in single-mode fibers," *Journal of Lightwave Technology*, vol. 1, no. 2, pp. 312–331, 1983.

[37] G. P. Agrawal, "Nonlinear fiber optics," in *Nonlinear Science at the Dawn of the 21st Century*, pp. 195–211, Springer, 2000.

[38] M. F. Ferreira, *Nonlinear effects in optical fibers*. John Wiley & Sons, 2011.

[39] R. A. Serway and J. W. Jewett, *Physics for scientists and engineers*. Cengage learning, 2018.

[40] H. Gong, H. Song, S. Zhang, K. Ni, and X. Dong, "An optical liquid level sensor based on polarization-maintaining fiber modal interferometer," *Sensors and Actuators A: Physical*, vol. 205, pp. 204–207, 2014.

[41] H. H. Qazi, A. B. Mohammad, H. Ahmad, and M. Z. Zulkifli, "D-shaped polarization maintaining fiber sensor for strain and temperature monitoring," *Sensors*, vol. 16, no. 9, p. 1505, 2016.

[42] X. Zhu, W. Liu, D. Sun, G. Zhang, L. Zou, Z. Liang, Z. Han, and Y. Shi, "High-sensitive acoustic sensor based on microfiber mach–zehnder interferometer with tapered polarization-maintaining fiber," *Fiber and Integrated Optics*, pp. 1–21, 2022.

[43] H. C. Lefevre, *The fiber-optic gyroscope*. Artech house, 2022.

[44] V. Vali and R. Shorthill, "Fiber ring interferometer," *Applied optics*, vol. 15, no. 5, pp. 1099–1100, 1976.

[45] R. Bergh, H. Lefevre, and H. Shaw, "An overview of fiber-optic gyroscopes," *Journal of Lightwave Technology*, vol. 2, no. 2, pp. 91–107, 1984.

[46] Y. Günhan, "Ataletsel ölçüm birimi hatalarının belirlenmesi ve düzeltilmesi," 2014.

[47] G. Sagnac, "L'éther lumineux démontré par l'effet du vent relatif d'éther dans un interféromètre en rotation uniforme," *CR Acad. Sci.*, vol. 157, pp. 708–710, 1913.

[48] H. C. Lefevre, "Application of the sagnac effect in the interferometric fiber-optic gyroscope," *Optical Gyros and ther Application. Printed by Canada Communication Group Inc.(A. St. Joseph Corporation Company)*, vol. 45, 1999.

[49] M. N. Armenise, C. Ciminelli, F. Dell'Olio, and V. M. Passaro, *Advances in gyroscope technologies*. Springer Science & Business Media, 2010.

[50] E. Alaçakır, "Modeling of environmental temperature dependency for sensors operated by sagnac effect," Master's thesis, Middle East Technical University, 2019.

[51] P. Marten, K. Petermann, E. Weidel, R. Ulrich, *et al.*, "Low-drift fibre gyro using a superluminescent diode," *Electronics Letters*, vol. 10, no. 17, pp. 352–353, 1981.

[52] M. Heimann, M. Liesegang, N. Arndt-Staufenbiel, H. Schröder, and K.-D. Lang, "Optical system components for navigation grade fiber optic gyroscopes," in *Emerging Technologies in Security and Defence; and Quantum Security II; and Unmanned Sensor Systems X*, vol. 8899, pp. 223–231, SPIE, 2013.

[53] P. Morkel, "Erbium-doped fibre superfluorescent source for the fibre gyroscope," 1989.

[54] P. F. Wysocki, R. F. Kalman, M. J. Digonnet, and B. Y. Kim, "1.55-um broadband fiber sources pumped near 980 nm," in *Fiber Laser Sources and Amplifiers II*, vol. 1373, pp. 66–77, SPIE, 1991.

[55] A. Cordova, R. A. Patterson, E. L. Goldner, and D. M. Rozelle, "Interferometric fiber optic gyroscope with inertial navigation performance over extended dynamic environments," in *Fiber Optic and Laser Sensors XI*, vol. 2070, pp. 164–180, SPIE, 1994.

[56] X. Yi and X. Wen, "Y-integrated optic chip (y-ioc) applied in fiber optic gyro," in *Advanced Laser Technologies 2005*, vol. 6344, pp. 180–186, SPIE, 2006.

[57] D. M. Shupe, "Thermally induced nonreciprocity in the fiber-optic interferometer," *Applied optics*, vol. 19, no. 5, pp. 654–655, 1980.

[58] A. Ohno, S. Motohara, R. Usui, Y. Itoh, and K. Okada, "Development of fiber optic gyroscope with environmental ruggedness," in *Fiber Optic Gyros: 15th Anniversary Conf*, vol. 1585, pp. 82–88, SPIE, 1992.

[59] N. J. Frigo, "Compensation of linear sources of non-reciprocity in sagnac interferometers," in *Fiber Optic and Laser Sensors I*, vol. 412, pp. 268–271, SPIE, 1983.

[60] Z. Gao, Y. Zhang, and Y. Zhang, "Modeling for ifog vibration error based on the strain distribution of quadrupolar fiber coil," *Sensors*, vol. 16, no. 7, p. 1131, 2016.

[61] B. Osunluk, S. Ogut, and E. Ozbay, "Thermally induced bias error due to strain inhomogeneity through the fiber optic gyroscope coil," *Applied Optics*, vol. 59, no. 33, pp. 10416–10421, 2020.

[62] B. Osunluk, *Environmental Effects on Interferometric Fiber Optic Gyroscope Performance*. PhD thesis, Bilkent Universitesi (Turkey), 2021.

[63] A. Cordova, "Reduction of fiber optic gyroscope vibration and temperature-ramp sensitivities by controlling coil geometrical parameters," Dec. 8 1998. US Patent 5,847,829.

[64] F. Mohr and F. Schadt, "Bias error in fiber optic gyroscopes due to elasto-optic interactions in the sensor fiber," in *Second European Workshop on Optical Fibre Sensors*, vol. 5502, pp. 410–413, SPIE, 2004.

[65] K. Hotate and K. Tabe, "Drift of an optical fiber gyroscope caused by the faraday effect: influence of the earth's magnetic field," *Applied Optics*, vol. 25, no. 7, pp. 1086–1092, 1986.

[66] S. Ezekiel and H. J. Arditty, *Fiber-Optic Rotation Sensors and Related Technologies: Proceedings of the First International Conference MIT, Cambridge, Mass., USA, November 9–11, 1981*, vol. 32. Springer, 2013.

[67] Y. Zhao, Y. Zhou, D. Zhang, J. Yang, Y. Zhou, S. Shi, X. Shu, and C. Liu, "Nonreciprocal phase error caused by orthogonal magnetic field in a polarization-maintaining fiber-optic gyro," *IEEE Sensors Journal*, vol. 15, no. 9, pp. 5128–5132, 2015.

[68] K. Böhm, K. Petermann, and E. Weidel, "Sensitivity of a fiber-optic gyroscope to environmental magnetic fields," *Optics Letters*, vol. 7, no. 4, pp. 180–182, 1982.

[69] M. A. Olson, W. H. Williams, J. A. Vaught, and M. B. McEwen, "Magnetic shield for a fiber optic gyroscope," Oct. 4 2005. US Patent 6,952,268.

[70] Z. N. Wang, Y. Yang, P. Lu, Y. X. Li, C. Peng, Z. R. Zhang, and Z. B. Li, "Optical compensation for compressing polarization nonreciprocity induced errors in interferometric fiber-optic gyroscopes," in *Applied Mechanics and Materials*, vol. 303, pp. 82–85, Trans Tech Publ, 2013.

[71] P. Liu, X. Li, X. Guang, G. Li, and L. Guan, "Bias error caused by the faraday effect in fiber optical gyroscope with double sensitivity," *IEEE Photonics Technology Letters*, vol. 29, no. 15, pp. 1273–1276, 2017.

[72] Y. Yang, Z. Wang, and Z. Li, "Optically compensated dual-polarization interferometric fiber-optic gyroscope," *Optics Letters*, vol. 37, no. 14, pp. 2841–2843, 2012.

[73] Z. Wang, Y. Yang, P. Lu, R. Luo, Y. Li, D. Zhao, C. Peng, and Z. Li, "Dual-polarization interferometric fiber-optic gyroscope with an ultra-simple configuration," *Optics letters*, vol. 39, no. 8, pp. 2463–2466, 2014.

[74] P. Liu, X. Li, X. Guang, Z. Xu, W. Ling, and H. Yang, "Drift suppression in a dual-polarization fiber optic gyroscope caused by the faraday effect," *Optics Communications*, vol. 394, pp. 122–128, 2017.

[75] A. Yertutanol, Ö. Akçaalan, S. Öğüt, E. Özbay, and A. Ceylan, "Fiber-optic gyroscope for the suppression of a faraday-effect-induced bias error," *Optics Letters*, vol. 46, no. 17, pp. 4328–4331, 2021.

[76] Z. Fang, K. Chin, R. Qu, and H. Cai, *Fundamentals of optical fiber sensors*, vol. 226. John Wiley & Sons, 2012.

[77] R. A. Bergh, H. C. Lefevre, and H. J. Shaw, "Compensation of the optical kerr effect in fiber-optic gyroscopes," *Optics Letters*, vol. 7, no. 6, pp. 282–284, 1982.

[78] W. K. Burns, P. F. Liao, and P. Kelley, *Optical fiber rotation sensing*. Academic Press, 2012.

[79] K. Petermann, "Intensity-dependent nonreciprocal phase shift in fiber-optic gyroscopes for light sources with low coherence," *Optics Letters*, vol. 7, no. 12, pp. 623–625, 1982.

[80] J. M. Wheeler and M. J. Digonnet, "A low-drift laser-driven fog suitable for trans-pacific inertial navigation," *Journal of Lightwave Technology*, 2022.

[81] M. Islam and M. R. Saleem, "Composition-property correlation in b2o3-sio2 preform rods produced using modified chemical vapor deposition technique," *Journal of materials engineering and performance*, vol. 21, no. 2, pp. 202–207, 2012.

[82] G. W. Scherer, "Stress-induced index profile distortion in optical waveguides," *Applied Optics*, vol. 19, no. 12, pp. 2000–2006, 1980.

[83] F. Rukerandanga, S. Musyoki, and E. O. Ataro, "3d design and analysis of an electro-optically tunable athermal and polarization-insensitive ring resonator-based add-drop filter for dwdm systems," *Heliyon*, p. e09567, 2022.

[84] Z. Zhang, C. Zhang, and X. Xu, "Stress-induced phase sensitivity of small diameter polarization maintaining solid-core photonic crystal fibre," *Journal of Modern Optics*, vol. 64, no. 17, pp. 1739–1743, 2017.

[85] C. Xiao, G. Zhang, S.-y. Ma, W. Ji, L. Rong, Z.-y. Wang, J.-x. Qiu, C.-l. Xu, and Y.-j. He, "Birefringence of pm laser fibers with different structure," in *Fifth Symposium on Novel Optoelectronic Detection Technology and Application*, vol. 11023, pp. 895–899, SPIE, 2019.

[86] T. Hosaka, Y. Sasaki, K. Okamoto, and J. Noda, "Stress-applied polarization-maintaining optical fibers. design and fabrication," *Electronics and Communications in Japan (Part II: Electronics)*, vol. 68, no. 3, pp. 37–47, 1985.

[87] F. Tu, H. Wang, J. Luo, and D. Liu, "Development of pmf for high precision fiber optic gyroscope by pcvd based process," in *Passive Components and Fiber-based Devices III*, vol. 6351, pp. 180–184, SPIE, 2006.

[88] Coherent/Nufern, "1550 nm pm gyroscope and sensor fibers." https://content.coherent.com/pdf/pm1550g_80_135_2hp_spec_202011122146.pdf, Accessed: February, 2023.

[89] Corning, "Corning/specialty materials/specialty optical fibers/panda pm pi sheet-m0500017/apr 2014." https://corning.com/media/worldwide/csm/documents/PANDA%20PM%20and%20RC%20PANDA%20Specialty%20Fiber.pdf, Accessed: February, 2023.

[90] S. Thirumeni, P. Poopalan, A. Hassan, and H. Ahmad, "Effects of scan angles in the far-field scanning method on the measurement of the mode field

diameter," in *ICSE'98. 1998 IEEE International Conference on Semiconductor Electronics. Proceedings (Cat. No. 98EX187)*, pp. 121–123, IEEE, 1998.

[91] E.-G. Neumann, *Single-mode fibers: fundamentals*, vol. 57. Springer, 2013.

[92] S. Gangopadhyay and S. Sarkar, "Evaluation of modal spot size in single-mode graded index fibers by a simple technique," *Journal of optical communications*, vol. 19, no. 5, pp. 173–175, 1998.

[93] E. Y. Yıldırım, A. Karatutlu, E. T. Balk, Y. Midilli, and B. Ortaç, "Combined method for the fabrication of high-power cladding light stripper using a buffered oxide etchant," *Applied Optics*, vol. 58, no. 25, pp. 6926–6933, 2019.

[94] YOFC, "Polarization maintaining fibre series (pmf)." https://en.yofc.com/view/2293.html, Accessed: February, 2023.

[95] B. Culshaw and A. Kersey, "Fiber-optic sensing: A historical perspective," *Journal of lightwave technology*, vol. 26, no. 9, pp. 1064–1078, 2008.

[96] M. Lenner, L. Yang, A. Frank, and K. Bohnert, "Long-term reliability of fiber-optic sensor components in harsh industrial environments," in *Optical Sensors*, pp. SeW1E–3, Optica Publishing Group, 2017.

[97] L. Teng, J. Yan, Y. Dong, and T. Guo, "Identification the differences of phase and group birefringence of different polarization-maintaining fibers with brillouin dynamic grating and sagnac interferometer," in *2018 IEEE International Instrumentation and Measurement Technology Conference (I2MTC)*, pp. 1–5, IEEE, 2018.

[98] R. Stevens, "Polarisation extinction ratio-measurement requirements for optical communication systems.," 2002.

[99] C. Jiang, Y. Liu, and C. Mou, "Polarization-maintaining fiber long-period grating based vector curvature sensor," *IEEE Photonics Technology Letters*, vol. 33, no. 7, pp. 358–361, 2021.

[100] Thorlabs, "Polarization-maintaining fiber: Panda style." https://www.thorlabs.com/drawings/fa3003d9cb5fdd8c-98B34FA1-EF47-9D19-F03CE84D6E79E311/PM1550-XP-SpecSheet.pdf, Accessed: February, 2023.

[101] iXblue, "ixblue photonics." https://www.ixblue.com/wp-content/uploads/2022/02/IXF-PMG-1550-80-P019_edB_polarization_maintaining_gyroscope_fiber.pdf, Accessed: February, 2023.

[102] OFS, "Gyrosil® 1550-155 polarization-maintaining optical fiber p/n: 27322." https://fiber-optic-catalog.ofsoptics.com/documents/pdf/27322-GyroSil-1550-155-Polarization-Maintaining-Optical-Fiber-web.pdf, Accessed: February, 2023.

[103] OFS, "Gyrosil® 1550-135 polarization-maintaining optical fiber p/n: 35889." https://fiber-optic-catalog.ofsoptics.com/documents/pdf/35889-GyroSil-1550-135-Polarization-Maintaining-Optical-Fiber-web.pdf, Accessed: February, 2023.

[104] N. FiberCore, "Standard gyro fiber." https://fibercore.humaneticsgroup.com/products/polarization-maintaining-pm-fiber/pm-gyro-fiber/standard-gyro-fiber/hb1500g-hi, Accessed: February, 2023.

[105] N. FiberCore, "Radiation tolerant fiber." https://fibercore.humaneticsgroup.com /products/polarization-maintaining-pm-fiber/pm-gyro-fiber/radiation-tolerant-fiber/hb1500g-rt, Accessed: February, 2023.

Appendix A

The specifications of the commercial PM fibers

The **Table A:1** was tabulated by following these information [88, 89, 94, 100–105]

Table A.1: The specifications of the commercial PM fibers

Fiber Brand	**Thorlabs**	**iXblue**	**Corning**		**OFS**	
Fiber Product	PM1550-XP	IXF-PMG-1550-80-P019	RC PM 1550	PM 1500	GyroSil 1550-155	GyroSil 1550-135
Operating Wavelength (nm)	1440 - 1625	1500 - 1600	1550	1550	1550	1550
Core Diameter (μm)	8.5					
Cladding Diameter (μm)	125 ± 2	80.0 ± 1.0	80.0 ± 1.0	125 ± 1	80.0 ± 1.0	80.0 ± 1.0
MFD @ 1550 nm (μm)	10.1 ± 0.4	6.7 ± 0.5	9.5 ± 0.5	10.5 ± 0.5	6.4 ± 0.5	6.4 ± 0.5
NA	0.125	0.19 ± 0.02				
Attenuation @ 1550 nm (dB/km)	1.0	1.0	2.0	0.5	1.0	1.0
Cut-off Wavelength (nm)	1380 ± 60	1480	1290 - 1450	1300 - 1440	1500	1500
Beat Length (mm)	5.0	1.6	2.5 - 4.5	3.0 - 5.0	3.5	3.5
Cross Talk @1550 nm (dB)	-40 dB @ 4 m		-25 @ 100 m	-30 @ 100 m		
Operating Temperature Range (C°)	-40 to +85	-40 to +85	-40 to +85	-40 to +85		
Proof Test Level (kpsi)	200	100	100	100	100	100

Fiber Brand	**Coherent/Nufern**		**YOFC**		**Newport**	**FiberCore**
Fiber Product	PM1550G-80/135-2HP	PM1550G-80/170-5	PM1550 80-18/165	PM1550 80-18/135	HB1500G	HB1500G-HI
Operating Wavelength (nm)	1520 - 1620	1520 - 1620	1550	1550	1520 - 1650	1520 - 1650
Core Diameter (μm)	6	6				
Cladding Diameter (μm)	80.0 ± 1.0	80.0 ± 1.0	80.0 ± 1.0	80.0 ± 1.0	80.0 ± 1.0	80.0 ± 1.0
MFD @ 1550 nm (μm)	6.3 ± 0.5	6.3 ± 0.5	6.5 ± 1.0	6.5 ± 0.	6.9 - 9.3	6.0 - 6.9
NA	0.19	0.19			0.14 - 0.18	0.19 - 0.21
Attenuation @1550 nm (dB/km)	1.0	2.0	0.8	0.8	2	3
Cut-off Wavelength (nm)	1460 ± 60	1460 ± 60	1290 - 1520	1290 - 1520	1230 - 1520	1360 - 1520
Beat Length (mm)	1.2	1.2	3.5	3.0	1.5	1.5
Cross Talk @1550 nm (dB)	-25 @ 100 m	-25 @ 100 m	-30 @ 100 m	-25 @ 100 m		
Operating Temperature Range (C°)	-60 to +105	-60 to +105	-45 to +85	-45 to +85	-55 to +85	-55 to +85
Proof Test Level (kpsi)	100	100	100	100	100 or 200	100 or 200